Constraining the complex refractive index of ambient black carbon particles from their observed distribution of the complex forward-scattering amplitude

Nobuhiro Moteki[1,2], Sho Ohata[3,4], Atsushi Yoshida[5], Kouji Adachi[6]

[1]Department of Earth and Planetary Science, Graduate School of Science, The University of Tokyo, Tokyo, Japan
[2]Chemical Sciences Laboratory, National Oceanic and Atmospheric Administration, Boulder, Colorado, USA
[3]Institute for Space–Earth Environmental Research, Nagoya University, Nagoya, Aichi, Japan
[4]Institute for Advanced Research, Nagoya University, Nagoya, Aichi, Japan
[5]National Institute of Polar Research, Tachikawa, Tokyo, Japan
[6]Department of Atmosphere, Ocean, and Earth System Modeling Research, Meteorological Research Institute, Tsukuba, Japan

Correspondence to: Nobuhiro Moteki (nobuhiro.moteki@gmail.com)

Abstract. Black carbon is the largest contributor to global aerosol's shortwave absorption in the current atmosphere and is one of the important positive climate forcers. The complex refractive index $m = m_r + im_i$, the primary determinant of the absorbed and scattered energies of incident radiation per unit volume of particulate material, has not yet been accurately known for atmospheric black carbon material. An accurate estimate of its refractive index at visible wavelengths has been difficult due to the wavelength-scale irregularity and variability of aggregate shape, distribution in particle size, and mixing with other aerosol compounds of ambient black carbon. Here, we propose an experimental method to constrain a plausible (m_r, m_i) domain of ambient black carbon from the observed distribution of the complex forward-scattering amplitude $S(0^\circ)$, which is designed to suppress the bias due to the above-mentioned complexities. The $S(0^\circ)$ distribution of ambient black carbon is acquired by performing single particle $S(0^\circ)$ measurements in a water medium after the collection of aerosols into water. We demonstrate the method operating at λ = 0.633 μm for constraining the refractive index of ambient black carbon over the north-western Pacific. From the observations, we suggest a conservative (m_r, m_i) domain that encloses the complex refractive index of ambient black carbon: $1.5 \le m_\mathrm{r} \le 2.3$ and $\max(0.25, 1.1m_\mathrm{r} - 1.6) \le m_\mathrm{i} \le \min(1.5, 2.5m_\mathrm{r} - 3.5)$. Despite the constrained (m_r, m_i) domain includes the current most popular assumption 1.95+0.79i, it does not exclude the possibility of higher m_i values.

1 Introduction

Black carbon (BC) emitted as a byproduct of the combustion of fossil fuels and biomasses, is one of the major anthropogenic contributors to positive climate forcing (Bond et al. 2013). In the present atmosphere, BC is estimated to have the largest contribution to global aerosol shortwave absorption (Samset et al. 2018; Sand et al. 2021). In climate simulations, the remaining large uncertainty in aerosol shortwave absorption is considered to dominate the prediction uncertainty of precipitation (Samset 2022). The BC is estimated to be the second largest contributor to positive effective radiative forcing among all greenhouse gases and aerosols over the Arctic, mainly due to the effects of BC deposition on snow on surface albedo reduction (Oshima et al. 2020).

Freshly emitted BC particles rapidly undergo internal mixing with other major aerosol components (e.g., sulfate, organics, water) through coagulation, condensation, and cloud processing and form BC-containing particles (Wang et al. 2017; Adachi et al. 2014; 2021). Here, we use the term BC to refer to strongly light-absorbing insoluble carbonaceous material (Bond et al. 2013), which will be more rigorously defined as "ns-soot" according to electron microscopic analyses (Buseck et al. 2014) or as "soot-BC" according to the classification of ambient light-absorbing carbonaceous particles by Corbin et al. (2019). In this paper, we use the terms "BC particles", and "BC aggregates" interchangeably to refer to an isolated particle consisting of BC material only, being distinguished from the BC-containing particles. Single ambient BC particles were observed to be a fractal-like aggregate of nanospheres (Bond et al. 2013). The nanosphere diameters are typically 10–100 nm (Buseck et al. 2014).

For such nonspherical BC aggregates, numerical light-scattering solvers, such as the superposition T-matrix method (STM) and discrete dipole approximation (DDA), are needed to theoretically predict its optical properties. The mass absorption cross-section (MAC) of BC aggregates was predicted to be only weakly sensitive to the morphological parameters of aggregate (e.g., fractal dimension, monomer size), but strongly sensitive to the refractive index of BC material (Liu and Mishchenko 2005). In climate modeling, basic assumptions on the BC refractive index therefore play a key role in aerosol shortwave absorption (Stier et al. 2007).

The refractive index $m_r + im_i$ of ambient BC at visible wavelengths is often assumed to be either of the followings: i) the highest recommended value for "light-absorbing carbon" at λ = 0.55 μm by Bond and Bergstrom (2006), 1.95+0.79i (BB06-h); ii) the lowest recommended value for light-absorbing carbon at λ = 0.55 μm by Bond and Bergstrom (2006), 1.75+0.63i (BB06-l); and iii) the wavelength-dependent $m_r + im_i$ value experimentally determined for propane-air flame soot by Chang and Charalampopoulos (1990) (CC90), which is, for example, 1.74+0.59i at λ = 0.55 μm. In practical uses of the BB06-h and BB06-l, the BC refractive index is assumed to be wavelength independent. Table 1 shows a non-exhaustive list of recent publications on atmospheric sciences that used any of the BB06-l, BB06-h, and CC90.

The wavelength-dependent BC refractive index from the Optical Properties of Aerosols and Clouds (OPAC) database (Hess et al. 1998), which is 1.75+0.44i at λ = 0.55 μm, is still used in some climate models (Sand et al. 2021), even

though it was formally not recommended by Bond and Bergstrom (2006) because of the ambiguity of experimental evidence. We therefore do not include the OPAC value in our discussion.

The recommended values at λ = 0.55 μm by Bond and Bergstrom (2006), BB06-h and -l, were determined based on the hypothetical "upper void-fraction line" on the (m_r, m_i) plane, which is a linear extrapolation of available experimental values for non-graphitic light-absorbing carbon, including CC90, toward a point of intersection with the hypothetical "graphitization line". The intersection point was defined to be BB06-h, which is not close to any experimental data. The BB06-l is close to the CC09 at λ = 0.55 μm as it was used as the uppermost datapoint to draw the void-fraction line.

Chang and Charalampopoulos (1990) experimentally determined the wavelength-dependent $m_r + im_i$ value of a propane-air flame soot, CC90, by applying the Kramers-Kronig dispersion theory to the measured spectral extinction coefficient of suspended soot particles over λ = 0.2–6.4 μm, under the observationally constrained particle-size distribution. The particle-size distribution was estimated using the photon-correlation technique at 0.488 μm wavelength (dynamic light-scattering). Chang and Charalampopoulos (1990) used the spherical particle-shape assumption in their interpretations of the spectral extinction and dynamic light-scattering data, possibly due to the unavailability of theoretical methods that account for more realistic shapes at that time. The spherical particle assumption to soot particles, the morphology of which is known to be an aggregate of nanospheres, might lead to a biased inference of spectral refractive index. Chang and Charalampopoulos (1990) mentioned that their derived refractive index should be regarded as an "effective" refractive index subject to their specific assumptions.

There have also been many other experimental studies on BC refractive index (cf. Table 4 and Fig. 7 of Bond and Bergstrom 2006). Some of them are based on the extinction spectroscopy of suspended particles as Chang and Charalampopoulos (1990), but with either less detailed experimental design or less detailed theoretical analyses. Others are based on the reflectance spectroscopy of a compressed pellet of powder sample or reflectance and transmission spectroscopy of particles collected on a plate. In the compressed-pellet approach, the wavelength-scale inhomogeneity of the surface and sub-surface matrix, which is difficult to quantify, should affect the reflected electromagnetic field (Ramezanpour and Mackowski 2019). In the on-plate approach, near-field electromagnetic interaction between deposited particles and plate, as well as neighboring particles affects the reflected and transmitted fields (Mackowski 2008). None of the previous compressed-pellet or on-plate approaches quantitatively discussed these near-field effects on their experimental setup.

Despite the prevalent use of BB06-h, BB06-l, and their average in recent climate models (Brown et al. 2021; Sand et al. 2021), their validities have not yet been confirmed by laboratory studies. Liu et al. (2020) pointed out in their review that light-scattering calculations assuming refractive indices of either BB06-h and BB06-l underpredict the measured MAC of uncoated BC aggregates at λ = 0.55 μm by ~30%, even though numerically exact solvers for an aggregate of nanoparticles are used. This discrepancy is considered to be caused by either or both the inaccurate morphological model and inaccurate refractive index assumed in the calculations. Liu et al. (2020) concluded that further explorations of the refractive index of BC materials are still needed.

All the earlier explorations of the refractive index of BC materials used synthetic samples (e.g., propane-air flame soot) rather than real-world aerosol samples, in part, because the previous experimental explorations of BC refractive index were mostly aimed at combustion science (Bond and Bergstrom 2006). It is usually difficult to apply the experimental methods designed for the high-concentration pure BC suspension in combustion studies to low-concentration mixed BC suspension in atmospheric studies. As the BC refractive index is considered to increase with the degree of graphitization (Stagg and Charalampopoulos 1993; Bond and Bergstrom 2006), the refractive index of ambient BC might depend on the emission source and its physicochemical environment of combustion (e.g., temperature, oxygen mixing ratio). Therefore, the refractive index of a synthetic BC material, even if it is accurately determined, would not be always applicable to predict the optical properties of ambient BC. Furthermore, the particle shape of ambient BC, which should be crucial information to obtain an unbiased estimate of its refractive index from any optical measurements, is variable depending on environmental and aging conditions (Bhandari et al. 2019).

We propose here a novel method for observationally constraining the complex refractive index of ambient BC largely avoiding the use of hypothetical assumptions that could lead to substantial bias. In this method, the complex scattering amplitude sensing technique (Moteki 2021) was used for optically identifying and characterizing single water-insoluble particles collected from ambient air. Then, Bayesian data analysis for refractive index inference is applied to the measured distribution of complex scattering amplitude of waterborne BC aggregates, which is distinguishable from the distributions of other water-insoluble aerosol components (e.g., mineral dust, organics). Effects of aggregate shape and particle-size distribution were also taken into account. In Sect. 2, we describe the method for complex scattering amplitude measurements and Bayesian data analyses. In Sect. 3, we describe the synthetic samples used for laboratory tests and the field observation of ambient aerosols. Results and discussion are presented in Sect. 4 followed by conclusions in Sect. 5.

2 Methods

In this section, we describe the complex amplitude sensor (CAS) used for the optical characterization of single waterborne BC and other particles (Sect. 2.1), followed by the Bayesian inverse model used for estimating the refractive index from the complex amplitude data (Sect. 2.2). An aerosol-into-water collection system that was connected to the CAS instrument for ambient aerosol measurements will be described Sect. 3.2.

2.1 Complex amplitude sensor

The complex scattering amplitude $S = |S|e^{i\Delta} \equiv \mathrm{Re}S + i\,\mathrm{Im}S$ is defined to describe the amplitude ratio $|S|$ and phase lag Δ of scattered field relative to the incident field. The self-reference interferometry (Giglio and Potenza 2011; Potenza et al. 2015) with a refined measurement protocol "Complex Amplitude Sensing version 1 (CAS-v1)" defined by Moteki (2021) was used to measure the complex forward-scattering amplitude $S(0^\circ)$ of single waterborne particles. Figure 1 shows the schematics of our complex amplitude sensor (CAS). The amplitude and phase of the forward-scattered field from each

waterborne particle illuminated by a focused Gaussian beam were retrieved from the interferometric power density modulation over the Gaussian beam's cross-section monitored by a quadrant photodiode (QPD). A linearly polarized ~2 mW He-Ne laser operated at λ = 0.6328 μm vacuum wavelength was used as the source of a clean Gaussian beam. The optical systems of the s- and l-channels were respectively designed to optimize the detection of sub- and super-micron-sized particles: the beam-waist spot size at the center of the sample flow channel was 2.90 μm and 12.4 μm for the s- and l-channels, respectively. Scattering particles with diameters up to ~1 μm (~4 μm) satisfy the validity criteria of the plane wave approximation of the incident Gaussian beam in the s-channel (l-channel) (Moteki 2021). The reference photodetector was used to cancel the laser noise from the QPD signals. Other details of this instrument, including procedures of tuning flow cell position and the method for processing the QPD signal waveforms to derive the $S(0^\circ)$ value, were fully described in Moteki (2021). As this instrument uses a linearly polarized Gaussian beam, the measured $S(0^\circ)$ value is one of the two diagonal elements of the 2x2 complex amplitude matrix, say, S_{22} following the coordinate convention of Moteki (2020).

2.2 Inversion of complex amplitude data

A unique particulate material forms a dense cluster of $S(0^\circ)$ data points on the complex plane that reflects its refractive index, shape, and size distribution ((Potenza et al. 2017; Moteki 2020; Yoshida et al. 2022). Each of the coexisting particulate materials suspended in an environmental fluid sample is broadly distributed in size and therefore tends to form a linear-or-curve-shaped elongated cluster of $S(0^\circ)$ data points. As to be demonstrated in Sect. 4, an elongated $S(0^\circ)$ cluster of ambient BC aggregates is distinguishable from those of the other water-insoluble aerosol components. Our aim is an unbiased inference of microphysical properties of BC aggregates, including refractive index, from an identified elongated cluster of $S(0^\circ)$ data points.

We used a computational Bayesian inference approach to solve this inverse problem, which can be ill-conditioned depending on the observation data. The Bayesian inference needs a forward model to compute the particle's $S(0^\circ)$ value from its microphysical parameters. We developed efficiently computable exact $S(0^\circ)$ forward model for an aggregate of nanospheres, as detailed below, and used it to execute a Bayesian inference.

2.2.1 Forward models

A design of exact but computable forward models for an aggregate of nanospheres requires an understanding of the physical link between $S(0^\circ)$ and particle's microphysical properties. For any single-component particles, $S(0^\circ)$ is only a function of the three factors: particle refractive index relative to the surrounding medium, particle volume, and the internal-to-incident field contrast averaged over the particle's volume (Moteki 2020). Particle shape affects $S(0^\circ)$ only through the last factor, which is interpreted as the ease of penetrating the incident field into the particle's volume. The incident field penetration to the entire volume of an aggregate is easier if the arrangement of monomers is less compact in terms of the outer envelope and/or internal structure (e.g., Beeler and Chakrabarty 2022). As ambient BC aggregates should have considerable diversity

in compactness of shape (Bhandari et a. 2019), an unbiased estimate of BC refractive index from $S(0^\circ)$ observation needs to take into account the possible variations of compactness of the BC aggregates.

The fractal model of an aggregate of spherical monomers with variable fractal dimension, commonly used for flame-soot studies, may be useful to parametrize the variation of compactness of fresh BC aggregates just after emission. However, it may not be practical to resolve the variation of compactness of aged BC aggregates that have experienced a collapse of the original lacy structure (Bhandari et al. 2019; Corbin et al. 2022). In addition to the shape model for a lacy aggregate, we used here another shape model for a compact aggregate that can parametrize the variation of packing density of monomers within its compact envelope.

The two shape models, listed in Table 2, are respectively defined as 1) a fractal-like aggregate of nanospheres with fractal prefactor 1.0 and fractal dimension 2.0–2.5 (AGGREGATE), and 2) a cluster of nonoverlapping nanospheres randomly positioned within a spherical volume with packing density 0.05–0.30 (SPHPACK). The spherule radius r_{pp} was fixed to 0.030 μm and the number of spherules N_{pp} was varied over 4–16384 in each shape model. The variable range of volume-equivalent radius r_v of aggregate was 0.048–0.76 μm. The AGGREGATE model parametrizes the variability of the projected area of a lacy aggregate by the fractal dimension, whereas the SPHPACK model parametrizes the variability of the internal porosity of a compact aggregate by the packing density. Each model BC particle has a set of parameter values $(r_v, m_r, m_i, \theta_s)$ within the parameter range listed in Table 2, where the shape parameter θ_s represents either fractal dimension (AGGREGATE) or packing density (SPHPACK). Examples of the AGGREGATE and SPHPACK models at N_{pp} = 1024 were shown in Figure 2.

We used the Multi-Sphere T-Matrix method (Mackowski and Mishchenko 2011) to predict $S(0^\circ)$ values of AGGREGATE and SPHPACK models in water medium as a function of $(r_v, m_r, m_i, \theta_s)$, under illumination by the plane wave of 0.633 μm vacuum wavelength. The original MSTM-v3.0 fortran90 code was modified to output the $S(0^\circ)$. Runtime calls of the MSTM as a forward model from a Bayesian inversion code are infeasible: even single MSTM-v3.0 run for typical wavelength-scale aggregates consisting of ~10^4 monomers will take several hours on a parallel computer cluster.

As a workaround strategy, we precomputed the $S(0^\circ)$ values over the discrete grid points of the parameter vector $(r_v, m_r, m_i, \theta_s)$ through lengthy MSTM runs, and then generated its spline interpolation function as a forward model for the Bayesian inversion. The parameter range and the number of grid points of $(r_v, m_r, m_i, \theta_s)$ were also shown in Table 2. The statistical error of the computed $S(0^\circ)$ value due to the aggregate's shape and orientation was mitigated by averaging the MSTM results for 5 random aggregates. For each shape model, we performed ($13 \times 20 \times 16 \times 6$) grid points $\times$ 5 aggregates =124800 MSTM runs using the Oakbridge-CX supercomputer system of The University of Tokyo.

2.2.2 Data vector

The data vector for Bayesian inversion was prepared from an identified dense-elongated cluster of $S(0^\circ)$ data points of BC aggregates according to the following procedure. We applied the principal curve fit (Hastie and Stuetzle 1989) to the data

points within the dense-elongate $S(0^\circ)$ cluster and assumed that the volume-equivalent radius r_v increases with the arclength coordinate s of the principal curve whilst the material parameters (m_r, m_i, θ_s) are unique to the cluster. We constructed a data vector $\vec{S}(0^\circ)$ from the principal curve projected $S(0^\circ)$ data points at the 0th, 5th, … , and 100th percentiles of s value. The data vector $\vec{S}(0^\circ)$ consisting of 21 complex scalar data (42 degrees of freedom) was used for the Bayesian inference of the model parameter vector $(\vec{r}_v, m_r, m_i, \theta_s)$ that is consisting of the 21 r_v parameters and the 3 material parameters (24 degrees of freedom). The principal curve projection followed by a selection of data points with every 5th percentile s interval realizes a reduction of the original data dimension to a constant number 21 without losing the observational information on the cluster's 1D shape and local density of the data points. Such dimensional reduction is important as the execution time of the Bayesian inference algorithm, described below, is proportional to the dimension of the data vector.

2.2.3 Bayesian inversion

We used the Hamiltonian Monte Carlo and No-U-Turn sampler (Hamiltonian-MC NUTs; Hoffman and Gelman 2014) accessible through the NumPyro probabilistic programing language (Phan et al. 2019), which attains much faster and more stable convergence than the previous approach (Moteki 2020) that used the random-walk MCMC method with the Metropolis-Hastings sampler (Hastings 1970). The likelihood function for Hamiltonian-MC NUTs was defined as follows. Each element of data vector $\vec{S}(0^\circ)$ was assumed to multivariate normally distributed around the $\vec{S}^*(0^\circ)$, where $\vec{S}^*(0^\circ)$ is the prediction from $(\vec{r}_v, m_r, m_i, \theta_s)$ by the forward model. The covariance matrix of the multivariate normal distribution was assumed to be a diagonal matrix reflecting the $S(0^\circ)$-measurement error in the s-channel. The measurement error was set to be $0.07S(0^\circ) + 0.02$ μm, a conservative estimate including both systematic and random errors (Moteki 2021). We assumed a uniform distribution within the parameter domain (Table 2) as the prior for $(\vec{r}_v, m_r, m_i, \theta_s)$.

Figure 3 illustrates the entire procedure for computing the Bayesian posterior (m_r, m_i) of BC aggregates from an identified dense-elongated cluster of $S(0^\circ)$ data points.

3 Samples

We applied the Bayesian inversion procedure described in Sect. 2 to each $S(0^\circ)$ cluster obtained for laboratory test samples and ambient aerosol samples suspended in water. The details of the laboratory samples and the field measurement of ambient aerosols are described in Sect. 3.1 and 3.2., respectively.

3.1 Laboratory test samples

Table 3 lists the four laboratory test samples used here. Transmission electron microscope (TEM) images of these powder materials were shown in Figure 4. The Fullerene Soot and Vehicle Exhaust Particulates, which contain ambient BC-like particulate materials, were selected for testing the applicability of our method to different types of BC aggregates. Fullerene

Soot is a synthetic BC powder material provided by Alfa Aesar Inc., which has been selected as a soot standard reference material for calibrating the single-particle BC measurements by laser-induced incandescence (Baumgardner et al. 2012) because of the closer resemblance of its incandescence-to-mass relationship with ambient and diesel-exhaust BCs than other commercially available particulate carbon materials (Slowik et al. 2007; Moteki and Kondo 2010; Laborde et al. 2012). Individual Fullerene soot particles were relatively compact aggregates of near-spherical nanoparticles with monomer diameter ~20−50 nm, in which essentially all the attached monomer pairs were sintered (Figure 4a). The Vehicle Exhaust Particulates, one of the certified reference materials for environmental studies provided by the National Institute of Environmental Studies, Japan, is a refractory water-insoluble powder material from vehicle exhausts, which was collected from ambient air in a highway tunnel and then thermochemically purified and dried for long-term storage (Honda 2021 and references therein). Individual BC particles contained in the Vehicle Exhaust Particulates (Vehicle exhaust BC) were compact aggregates of near-spherical nanoparticles with monomer diameter ~10−40 nm, in which most of the attached monomer pairs were less sintered than the Fullerene soot.

The AGGREGATE and SPHPACK shape models (Table 2), non-sintered aggregates of nanospheres with a radius of 30 nm, are different from the actual shape of these laboratory test BC samples in nanoscale details. Nevertheless, these shape models will be able to emulate the projected area per unit volume and wavelength-scale averaged internal porosity, which largely determine the ease of penetration of incident field through the particle's volume that determines the shape effects on $S(0^\circ)$. Theoretical estimates of the sensitivity of Bayesian inversion results to nanoscale shape features (e.g., sintering) of the assumed model require huge efforts of additional scattering calculations (cf. Qin et al. 2022). Instead of performing such analyses, here, we are presenting each inversion result as a probable $(m_\mathrm{r}, m_\mathrm{i})$ domain rather than as a single $(m_\mathrm{r}, m_\mathrm{i})$ point (Sects. 4 and 5).

In addition to these two BC materials, two synthetic hematite (α-Fe_2O_3) powder materials from Kojundo Chemical Co. Ltd. (Hematite-KJ) and Toda Kogyo Co. (Hematite-TD), were also used to test the sensitivity of the Bayesian inversion result to the refractive index of light-absorbing material. The imaginary part of refractive index m_i of red-colored hematite is likely lower than that of black-colored BC at λ = 0.633 μm: the published experimental m_i value of hematite at this wavelength distributes from ~0.01 to ~0.2 (Schuster et al. 2016). The single particle morphology was substantially different between the two hematite samples. Individual particles in the Hematite-KJ were compact aggregates of nonspherical nanoparticles with monomer dimension < ~100 nm, in which essentially all the attached monomer pairs were severely sintered. The particles in Hematite-TD were compact aggregates of near-spherical nanoparticles with monomer diameter ~30−100 nm, in which most of the attached monomer pairs were not sintered.

The AGGREGATE and SPHPACK models (Table 2) will not be able to emulate either nanoscale or wavelength-scale averaged morphological features of Hematite-KJ. To minimize the bias of Bayesian inversion due to the inaccuracy of the shape model, we only used the $S(0^\circ)$ data points near the origin wherein the $S(0^\circ)$ is less sensitive to the particle shape, as detailed in Sect. 4.1.

3.2 Ambient aerosol samples

The continuous single particle $S(0^{\circ})$ measurements of water-insoluble aerosols in the oceanic atmosphere were conducted on the research vessel SHINSEI MARU (Figure S1) during a 2-week cruise over the north-western Pacific (39.4−42.0 N°, 141.5−148.7 E°) from July 15th −August 2nd in 2022. The ambient air was aspirated from an aerosol inlet on the deck (~10 m altitude from the sea surface, ~1.5 m altitude from the deck floor) and then directed into a homemade aerosol-into-water collection system inside a cabin through 1/2" O.D. conductive silicone tubing (Figure S2). The system continuously transfers aerosol particles from 30 L min^{-1} air into 2 mL min^{-1} water. The schematic diagram and operating principle of the aerosol-into-water collection system were described in Figure S3. The sample water was continuously transported to the CAS instrument through 1/16" O.D. PEEK tubing for $S(0^{\circ})$ measurements of water-insoluble aerosol particles (Figure S2). The water flow through the CAS instrument was driven by a peristaltic pump at the outlet of the aerosol-into-water collection system. The transport time of particles from the aerosol inlet to the CAS flow cells was ~5 minutes.

The current version of the aerosol-into-water collection system has imperfect and strongly size-dependent collection efficiency for submicron water-insoluble particles as shown in Figure S4a, due to the particle-size-dependent collection efficiency from air into water (Figure S4b) and the particle-material dependent transport efficiency of collected particles from the spiral condenser to the water outlet (Figure S4c). The collection and transport efficiencies of a particular particulate material (Polystyrene, Silica) were stable under a fixed operating condition. The size-dependent imperfect aerosol sampling efficiency does not affect the constraint of BC refractive index through Bayesian inversion of $S(0^{\circ})$ data.

We used only the CAS data continuously acquired during the 6 days from July 27th to August 1st avoiding periods of instrument troubles. The cluster identification and following analyses described in Figure 3 were performed to an ensemble of $S(0^{\circ})$ data points accumulated during 0−24 h local time each day. Figure S5 shows a frequency map of backward trajectories of air parcels observed during each 24 h accumulation period calculated using the NOAA HYSPLIT model (Stein et al. 2015; Rolph et al. 2017). Examples of TEM images of ambient submicron aerosols collected by an aerosol-impactor sampler were shown in Figure 5. The BC aggregates observed in every aerosol-impactor sample were mostly compact. They had likely experienced a collapse of their original lacy structure during transport from the sources. The majority of non-BC aerosol components were organics, sulfate, and their mixture. A substantial fraction of the BC particles were internally mixed with either or both of these components.

4 Results and Discussion

4.1 The complex amplitude data

We only analyzed the s-channel data in this work as any of our laboratory test samples and ambient BC particles were mostly distributed in the submicron size domain and their $S(0^{\circ})$-distribution were hardly observed in the l-channel. For each

sample, we discard the particle detection events with signal waveform width greater than its 50th percentile value to increase the precision of the derived $S(0^\circ)$ data (Moteki 2021), with a sacrifice of 50 % reduction of the number of data points.

4.1.1. Laboratory test samples

Figures 6 shows the scatterplot of the $S(0^\circ)$ data points observed for each of the laboratory test samples. For each of the Fullerene soot and Vehicle exhaust particulates (Figures 6a and b), the linear-shape dense cluster of $S(0^\circ)$ data points with $\mathrm{Im}S(0^\circ)/\mathrm{Re}S(0^\circ)$ ratio > ~1 is attributable to BC aggregates with a high imaginary part of refractive index (Moteki 2020). For Fullerene soot, the sparse cluster of data points with $\mathrm{Im}S(0^\circ)/\mathrm{Re}S(0^\circ)$ ratio < ~0.5, which will be attributable to non-absorbing particles, was excluded from the analyses. For Vehicle exhaust particulates, the curved-shape cluster of $S(0^\circ)$ data points with lower $\mathrm{Im}S(0^\circ)/\mathrm{Re}S(0^\circ)$ ratio, which will be attributable to water-insoluble refractory road dust particles (metallic oxides), was excluded from the analyses. For each of the Fullerene soot and Vehicle exhaust particulates, a principal curve fit was applied to the cluster of $S(0^\circ)$ data points of BC aggregates and every 5th percentile of the arclength coordinate *s* was selected to construct the input data vector for Bayesian inference (Figure 3).

For each of the Hematite-KJ and Hematite-TD (Figure 6c and d), the clustered $S(0^\circ)$ data points distribute more broadly as the increase of $|S(0^\circ)|$ beyond ~0.2 μm due to the pronounced effects of particle's shape and orientation. The $S(0^\circ)$ distribution at $|S(0^\circ)|$ > ~0.2 μm was appreciably broader in Hematite-KJ than Hematite-TD, reflecting their morphological difference (c.f., Figure 4). For single component but nonspherical particulate materials, the transition from tight to broad $S(0^\circ)$ cluster occurs when the particle size becomes large enough so that the mean internal field is quite sensitive to the details of particle's shape and orientation. The earlier transition to the broad cluster in Hematite-KJ around $|S(0^\circ)|$ ~0.2 μm is likely due to its more sintered morphology and/or asymmetric envelope shape. In both Hematite-KJ and Hematite-TD, we only used $S(0^\circ)$ data points with $|S(0^\circ)| < 0.15$ μm for principal curve fit and following analyses to mitigate the potential bias of Bayesian inversion due to the shape model assumptions.

4.1.2. Ambient aerosol samples

Figure 7 shows the scatterplot of $S(0^\circ)$ data points of ambient water-insoluble aerosols in each observation day. In either of the 6 days, the linear-shape dense cluster of $S(0^\circ)$ data points with $\mathrm{Im}S(0^\circ)/\mathrm{Re}S(0^\circ)$ ratio > ~1 was clearly distinguishable from other clusters with lower $\mathrm{Im}S(0^\circ)/\mathrm{Re}S(0^\circ)$ ratios (Figure 7). We suppose the former cluster is solely attributable to BC aggregates for the following three reasons. Firstly, the $S(0^\circ)$ cluster were similar to those of laboratory BC materials. Secondly, the number concentration of aggregates of magnetite nanoparticles, which could exhibit $S(0^\circ)$ distributions indistinguishable from BC aggregates, was reported to be several orders of magnitude lower than the BC aggregates in the lower troposphere around East Asia (Moteki et al. 2017). Thirdly, other ubiquitous aerosol components that can form the linear-shape dense cluster of $S(0^\circ)$ data points with $\mathrm{Im}S(0^\circ)/\mathrm{Re}S(0^\circ)$ ratio > ~1 are not known.

The patchy $S(0^\circ)$ clusters that appeared in each panel of Figure 7 are attributable to the size-standard Polystyrene (PS) spheres with refractive index 1.585+0i. The PS particles that had been attached to the inner surface of the aerosol-into-water collection system during the laboratory experiments were gradually detached during the observation.

A curved-shape dense $S(0^\circ)$ cluster with lower $\mathrm{Im}S(0^\circ)/\mathrm{Re}S(0^\circ)$ ratio below the PS patchy clusters was persistent throughout the 6 days. The water-insoluble non-BC materials responsible for this cluster were not investigated here. The clear separation between this non-BC cluster and the BC cluster on the complex $S(0^\circ)$ plane, as observed in each panel of Figure 7, implies that the number fraction of BC-containing particles consisting of BC material and the non-BC water-insoluble materials was negligible as compared to the nearly pure BC particles in the water medium. Otherwise, $S(0^\circ)$ data points with various $\mathrm{Im}S(0^\circ)/\mathrm{Re}S(0^\circ)$ ratio between the two extremes, depending on the BC volume fraction of the internal mixture, should also be frequently observed. This observational evidence supports the use of aggregate shape models without considering the internally mixed non-BC materials in our Bayesian inference of the refractive index of ambient BC.

It was previously observed around this region that most of the submicron aerosol particles were comparably hygroscopic as ammonium sulfate (Mochida et al. 2011). It was reported that the hygroscopicity of the coating materials on the BC core was similar to that of the compositions of BC-free submicron particles even in the less-aged urban plumes (Ohata et al. 2016). Therefore, it is no surprise if the coating materials on the BC core in our field observations were comparably hygroscopic with the ammonium sulfate and dissolved into the water through the aerosol-into-water collection procedure.

4.2 The refractive index

4.2.1. Laboratory test samples

Figure 8 shows the 90%, 50%, and 10% highest density credibility regions of the joint probability of $(m_\mathrm{r}, m_\mathrm{i})$ posterior pair obtained for each of the four laboratory test samples. The credibility region was displayed for each shape model assumption. Corresponding to Figure 8a-d, Figures S6-S9 show computed chains of the posterior sample and its density distribution of each element of the parameter vector $(\vec{r}_\mathrm{v}, m_\mathrm{r}, m_\mathrm{i}, \theta_\mathrm{s})$. The BB06-l and -h were also plotted in Figure 8 for comparison.

In both Fullerene soot and Vehicle exhaust BC, the shape parameter θ_s of the AGGREGATE model (fractal dimension) exhibited a skewed posterior distribution toward the upper boundary of the parameter domain [2.0, 2.5] (Figure S6 and S7), suggesting that the actual BC aggregates in these samples could be more compact than fractal-like aggregates with fractal dimension ~2.5. By contrast, the shape parameter θ_s of the SPHPACK model (packing density) exhibited single modal posterior distributions within the parameter domain [0.05, 0.30] (Figure S6 and S7). This means that the SPHPACK model can reproduce the observed shape of the $S(0^\circ)$ cluster more confidently than the AGGREGATE model. The preference of the SPHPACK model for these samples is also expected from the predominance of compact BC aggregates in their TEM images (Figure 4). From this discussion, the credibility region of $(m_\mathrm{r}, m_\mathrm{i})$ for the SPHPACK model is considered to be more plausible than that of the AGGREGATE model. The $(m_\mathrm{r}, m_\mathrm{i})$ credibility region for the SPHPACK model was

appreciably different between Vehicle exhaust BC and Fullerene soot, likely due to their difference in the degree of graphitization.

Both Hematite-KJ and Hematite-TD samples exhibited much lower m_i/m_r ratio than the BC samples. This contrast between hematite and BC is consistent with the difference in previously reported values of their refractive index (Schuster et al. 2016). The derived credibility regions of (m_r, m_i) were similar between Hematite-KJ and Hematite-TD despite their difference in particle morphology, as we had suppressed the sensitivity of inversion results to particle shape by using only small $|S(0^\circ)|$ data. As a result, the shape parameter θ_s was poorly constrained for these hematite samples (Figures S8 and S9).

4.2.2. Ambient BC

Figures 9, S10-S15 show the same results as Figures 8, S6-S9 but for ambient BC. The credibility regions of (m_r, m_i) for ambient BC samples were closer to those of Vehicle exhaust BC rather than Fullerene soot. In any of the 6-day ambient BC samples, the shape parameter θ_s of the AGGREGATE model showed skewed posterior distribution toward the upper boundary of the parameter domain, while that of the SPHPACK model showed single modal distribution within the parameter domain (Figures S10-S15). These Bayesian inference results, as well as the predominance of relatively compact BC aggregate in TEM images of ambient aerosol samples (Figure 5), suggest that the SPHPACK model is more plausible than the AGGREGATE model for these ambient BC samples. The posterior mode of packing density θ_s of the SPHPACK model was larger on the July 28th sample ($\theta_s \sim 0.2$) than the other 5-day samples ($\theta_s \sim 0.15$). According to the trajectories, July 28th data were predominantly influenced by the oceanic remote atmosphere around the western Pacific, whereas the July 27th and July 29th – August 1st data were more-or-less affected by Japanese and/or continental emission sources. The larger packing density θ_s of BC aggregates on July 28th is likely due to the further progression of aggregate compaction during their longer atmospheric residence time. In spite of the systematic shift of shape parameter of BC aggregates on July 28th, the 50 % highest credibility region of (m_r, m_i) of BC aggregates on July 28th was not appreciably different from those of the other 5-days. This illustrates that our approach is able to suppress the bias of refractive index estimation due to the change in compactness of BC aggregates in the atmosphere. The 50 % highest credibility region of (m_r, m_i) always contained the BB06-l and h values during the 6 days. The 50 % highest credibility regions do not exclude the possibility of higher m_i values than BB06-h for both Vehicle exhaust and ambient BC samples, which might be related to the reported ~30% underestimate of measured MAC values by theoretical computations using the BB06-h (Liu et al. 2020 and references therein).

From the above results and discussion, we suggest a plausible (m_r, m_i) domain for ambient BC: $1.5 \leq m_r \leq 2.3$ and $\max(0.25, 1.1m_r - 1.6) \leq m_i \leq \min(1.5, 2.5m_r - 3.5)$. The borderlines of this domain were also plotted in Figure 9.

The inference uncertainty of the (m_r, m_i) of ambient BC, which was visualized as posterior distribution in Figure 9, is tightly correlated with the inference uncertainty of the volume-equivalent radii $\vec{r}_v$, as illustrated in Figure 10. This suggests

that the incorporation of the independently measured volume-equivalent size distribution of waterborne BC particles into the Bayesian inference procedure as additional data could help to reduce the inference uncertainty of the (m_r, m_i).

5 Conclusions

We developed a method for constraining the refractive index of ambient BC at visible wavelengths through single-particle measurements of complex forward-scattering amplitude $S(0^\circ)$, and demonstrated at λ = 0.633 μm. The $S(0^\circ)$ measurement of aerosol particles after collection into the water was shown to be effective to extract the $S(0^\circ)$ data points attributable to pure BC aggregates avoiding the influences of other ambient aerosol components. The simultaneous retrieval of particle's shape information from the $S(0^\circ)$ data was shown to be effective to suppress the bias of refractive index inference due to the variability of compactness of ambient BC aggregates. Our original estimates of (m_r, m_i) for ambient BC did not exclude the possibility of the conventional assumptions BB06-l (1.75+0.63i) and BB06-h (1.95+0.79i). We suggest that a conservative (m_r, m_i) domain that includes complex refractive index $m_r + im_i$ of ambient BC materials at 0.633 μm wavelength: $1.5 \leq m_r \leq 2.3$ and $\max(0.25, 1.1m_r - 1.6) \leq m_i \leq \min(1.5, 2.5m_r - 3.5)$. Any (m_r, m_i) values outside this domain are not recommended. Our results did not exclude the possibility of higher m_i than BB06-h at m_r~1.95.

Code availability

The originally developed Python module used for auto-differentiable multidimensional spline interpolation of gridded data is available from: https://github.com/nmoteki/ndimsplinejax. The code used for generating fractal-like aggregates of spheres is available from https://github.com/nmoteki/aggregate_generator. Other codes used for this study are available from the corresponding author upon reasonable request.

Data availability

Data generated for Figures 6 and 7 are available from: https://doi.org/10.5281/zenodo.7478889.

Sample availability

Samples used for this study (Fullerene soot, Vehicle Exhaust Particulates, Hematite-KJ, Hematite-TD) are available from the corresponding author upon reasonable request.

Supplement

The supplement related to this article is available online at:

Author contribution

NM designed the research, NM developed the instruments and codes, SO and AY operated instruments during the research cruise. KA performed TEM analyses of particle samples.

Competing interests

The contact author has declared that none of the authors has any competing interests.

ORCID

Nobuhiro Moteki,	https://orcid.org/0000-0001-7963-6690
Sho Ohata	https://orcid.org/0000-0002-6777-0662
Atsushi Yoshida	https://orcid.org/0000-0001-9784-2236
Kouji Adachi	https://orcid.org/0000-0002-2977-1728

Acknowledgments

We thank the Drs. Y. Kawai, M. Koike, T. Miyakawa, and JAMSTEC staff for supporting the atmospheric aerosol measurements using the research vessel SHINSEI MARU. The authors thank D. W. Mackowski for the provision of the MSTM code used in this publication. The authors thank S. Zhang for providing the "pcurvepy" Python module used for principal curve fit. The authors thank the NOAA Air Resources Laboratory (ARL) for the provision of the HYSPLIT transport and dispersion model and/or READY website (https://www.ready.noaa.gov) used in this publication.

Financial support

Funds were provided by the Environment Research and Technology Development Fund (JPMEERF20202003) of the Environmental Restoration and Conservation Agency, the Japan Society for the Promotion of Science (JSPS) KAKENHI program (JP19H04236, JP19KK0289, JP19H04259, JP19H05699, 22H03722, and 22H01294), and the Arctic Challenge for Sustainability ArCS II project (JPMXD1420318865) of the Ministry of Education, Culture, Sports, Science, and Technology (MEXT) of Japan.

References

Adachi, K., N. Oshima, S. Ohata, A. Yoshida, N. Moteki, and M. Koike. 2021. Compositions and mixing states of aerosol particles by aircraft observations in the Arctic springtime, 2018. *Atmos. Chem. Phys.* 21(5):3607–3626. doi:10.5194/acp-21-3607-2021.

Adachi, K., Y. Zaizen, M. Kajino, and Y. Igarashi. 2014. Mixing state of regionally transported soot particles and the coating effect on their size and shape at a mountain site in Japan. *J. Geophys. Res. Atmos.* 119(9):5386-5396. doi:10.1002/2013JD020880.

Baumgardner, D., Popovicheva, O., Allan, J., Bernardoni, V., Cao, J., Cavalli, F., Cozic, J., Diapouli, E., Eleftheriadis, K. Genberg, P. J. et al. 2012. Soot reference materials for instrument calibration and intercomparisons: a workshop summary with recommendations. *Atmos. Meas. Tech.* 5(8):1869-1887. doi:10.5194/amt-5-1869-2012.

Beeler, P. and R. K. Chakrabarty. 2022. Constraining the particle-scale diversity of black carbon light absorption using a unified framework. *Atmos. Chem. Phys.* 22(22):14825-14836. doi:10.5194/acp-22-14825-2022.

Bhandari, J., S. China, K. K. Chandrakar, G. Kinney, W. Cantrell, R. A. Shaw, L. R. Mazzoleni, G. Girotto, N. Sharma, K. Gorkowski et al. 2019. Extensive soot compaction by cloud processing from laboratory and field observations. *Sci. Rep.* 9:11824. doi:10.1038/s41598-019-48143-y.

Bond, T. C. and R. W. Bergstrom. 2006. Light absorption by carbonaceous particles: An investigative review. *Aerosol Sci. Technol.* 40(1):27-67. doi:10.1080/02786820500421521.

Bond, T. C., S. J. Doherty, D. W. Fahey, P. M. Forster, T. Berntsen, B. J. DeAngelo, M. G. Flanner, S. Ghan, B. Kärcher, D. Koch et al. 2013. Bounding the role of black carbon in the climate system: A scientific assessment. *J. Geophys. Res. Atmos.* 118(11): 5380-5552. doi:10.1002/jgrd.50171.

Brown, H., X. Liu, R. Pokhrel, S. Murphy, Z. Lu, R. Saleh, T. Mielonen, H. Kokkola, T. Bergman, G. Myhre et al. 2021. Biomass burning aerosols in most climate models are too absorbing. *Nat. Commun.* 12:277. doi:10.1038/s41467-020-20482-9.

Buseck, P. R., K. Adachi, A. Gelencsér, É. Tompa, and M. Pósfai. 2014. Ns-soot: A material-based term for strongly light-absorbing carbonaceous particles. *Aerosol Sci. Technol.* 48(7):777-788. doi:10.1080/02786826.2014.919374.

Chang, H. C. and T. T. Charalampopoulos. 1990. Determination of the wavelength dependence of refractive indices of flame soot. *Proc. R. Soc. Lond. A. Math. Phys. Sci.* 430(1880):577-591. doi:10.1098/rspa.1990.0107.

Cheng, T., X. Gu, Y. Wu, H. Chen, and T. Yu. 2013. The optical properties of absorbing aerosols with fractal soot aggregates: Implications for aerosol remote sensing. *J. Quant. Spectrosc. Radiat. Transfer*. 125:93-104. doi:10.1016/j.jqsrt.2013.03.012.

Corbin, J. C., H. Czech, D. Massabò, F. B. de Mongeot, G. Jakobi, F. Liu, P. Lobo, C. Mennucci, A. A. Mensah, J. Orasche et al. 2019. Infrared-absorbing carbonaceous tar can dominate light absorption by marine-engine exhaust. *npj Clim. Atmos. Sci.* 2(1):1-10. doi:10.1038/s41612-019-0069-5.

Corbin, J. C., R. L. Modini, and M. Gysel-Beer. 2022. Mechanisms of soot-aggregate restructuring and compaction. *Aerosol Sci. Technol.* Forthcoming. doi:10.1080/02786826.2022.2137385.

Giglio, M. and M. A. C. Potenza. 2011. Method of measuring properties of particles and corresponding apparatus. US Patent 7924431B2. issued April 12, 2011.

Hastie, T. and W. Stuetzle. 1989. Principal curves. *J. Am. Stat. Assoc.* 84(406):502-516. doi:10.2307/2289936.

Hastings, W. K. 1970. Monte Carlo sampling methods using Markov chains and their applications. Biometrika, 57(1):97–109. doi:10.1093/biomet/57.1.97.

Hess, M., P. Koepke, and I. Schult. 1998. Optical properties of aerosols and clouds: The software package OPAC. *Bull. Amer. Meteor. Soc.* 79(5):831-844. doi:10.1175/1520-0477(1998)079<0831:OPOAAC>2.0.CO;2.

Hoffman, M. D. and A. Gelman. 2014. The No-U-Turn sampler: adaptively setting path lengths in Hamiltonian Monte Carlo. *J. Mach. Learn. Res.*, 15(1):1593-1623.

Honda, M. 2021. Multielement quantification and Pb isotope analysis of the certified reference material ERM-CZ120 for fine particulate matter. *Geochem. J.* 55(6):355-371. doi:10.2343/geochemj.2.0642.

Kahnert, M. and A. Devasthale. 2011. Black carbon fractal morphology and short-wave radiative impact: a modelling study. *Atmos. Chem. Phys.* 11(22):11745-11759. doi:10.5194/acp-11-11745-2011.

Koike, M., N. Moteki, P. Khatri, T. Takamura, N. Takegawa, Y. Kondo, H. Hashioka, H. Matsui, A. Shimizu, and N. Sugimoto. 2014. Case study of absorption aerosol optical depth closure of black carbon over the East China Sea. *J. Geophys. Res. Atmos.* 119(1):122-136. doi:10.1002/2013JD020163.

Laborde, M., P. Mertes, P. Zieger, J. Dommen, U. Baltensperger, and M. Gysel. 2012. Sensitivity of the single particle soot photometer to different black carbon types. *Atmos. Meas. Tech.* 5(5):1031-1043. doi:10.5194/amt-5-1031-2012.

Li, L., O. Dubovik, Y. Derimian, G. L. Schuster, T. Lapyonok, P. Litvinov, F. Ducos, D. Fuertes, C. Chen, Z. Li et al. 2019. Retrieval of aerosol components directly from satellite and ground-based measurements. *Atmos. Chem. Phys.* 19(21):13409-13443. doi:10.5194/acp-19-13409-2019.

Liu, F., J. Yon, A. Fuentes, P. Lobo, G. J. Smallwood, and J. C. Corbin. 2020. Review of recent literature on the light absorption properties of black carbon: Refractive index, mass absorption cross section, and absorption function. *Aerosol Sci. Technol.* 54(1):33-51. doi:10.1080/02786826.2019.1676878.

Liu, L. and M. I. Mishchenko. 2005. Effects of aggregation on scattering and radiative properties of soot aerosols. *J. Geophys. Res. Atmos.* 110:D11211. doi:10.1029/2004JD005649.

Mackowski, D. W. 2008. Exact solution for the scattering and absorption properties of sphere clusters on a plane surface. *J. Quant. Spectrosc. Radiat. Transfer*. 109(5):770-788. doi:10.1016/j.jqsrt.2007.08.024.

Mackowski, D. W. and M. I. Mishchenko. 2011. A multiple sphere T-matrix Fortran code for use on parallel computer clusters. *J. Quant. Spectrosc. Radiat. Transfer*. 112(13):2182-2192. doi:10.1016/j.jqsrt.2011.02.019.

Moosmüller, H., R. K. Chakrabarty, and W. P. Arnott. 2009. Aerosol light absorption and its measurement: A review. *J. Quant. Spectrosc. Radiat. Transfer*. 110(11):844-878. doi:10.1016/j.jqsrt.2009.02.035.

Mochida, M., C. Nishita-Hara, H. Furutani, Y. Miyazaki, J. Jung, K. Kawamura, and M. Uematsu. 2011. Hygroscopicity and cloud condensation nucleus activity of marine aerosol particles over the western North Pacific. *J. Geophys. Res.* 116:D06204. doi:10.1029/2010JD014759

Moteki, N. 2020. Capabilities and limitations of the single-particle extinction and scattering method for estimating the complex refractive index and size-distribution of spherical and non-spherical submicron particles. *J. Quant. Spectrosc. Radiat. Transfer*. 243:106811. doi:10.1016/j.jqsrt.2019.106811.

Moteki, N. 2021. Measuring the complex forward-scattering amplitude of single particles by self-reference interferometry: CAS-v1 protocol. Opt. Express. 29(13):20688-20714. doi:10.1364/OE.423175.

Moteki, N. and Y. Kondo. 2010. Dependence of laser-induced incandescence on physical properties of black carbon aerosols: Measurements and theoretical interpretation. *Aerosol Sci. Technol.* 44(8):663-675. doi:10.1080/02786826.2010.484450.

Moteki, N., K. Adachi, S. Ohata, A. Yoshida, T. Harigaya, M. Koike, and Y. Kondo. 2017. Anthropogenic iron oxide aerosols enhance atmospheric heating. *Nat. Commun.* 8:15329. doi:10.1038/ncomms15329.

Ohata, S., J. P. Schwarz, N. Moteki, M. Koike, A. Takami, and Y. Kondo. 2016. Hygroscopicity of materials internally mixed with black carbon measured in Tokyo. *J. Geophys. Res. Atmos.* 121:362–381. doi:10.1002/2015JD024153

Oshima, N., S. Yukimoto, M. Deushi, T. Koshiro, H. Kawai, T. Y. Tanaka, and K. Yoshida. 2020. Global and Arctic effective radiative forcing of anthropogenic gases and aerosols in MRI-ESM2.0. *Prog. Earth Planet. Sci.* 7:38. doi:10.1186/s40645-020-00348-w.

Phan, D., N. Pradhan, and M. Jankowiak. 2019. Composable effects for flexible and accelerated probabilistic programming in NumPyro. arXiv preprint. arXiv:1912.11554. doi:10.48550/arXiv.1912.11554.

Potenza, M. A., T. Sanvito, and A. Pullia. 2015. Measuring the complex field scattered by single submicron particles, *AIP Adv.* 5(11):117222. doi:10.1063/1.4935927.

Potenza, M. A. C., Ž. Krpetić, T. Sanvito, Q. Cai, M. Monopoli, J. M. De Araujo, C. Cella, L. Boselli, V. Castagnola, P. Milani et al. 2017. Detecting the shape of anisotropic gold nanoparticles in dispersion with single particle extinction and scattering. *Nanoscale*. 9(8):2778-2784. doi:10.1039/C6NR08977A.

Qin, Z., Zhang, Q., Luo, J., and Zhang, Y. 2022. Optical properties of soot aggregates with different monomer shapes. Environ. Res. 214(2):113895. doi:10.1016/j.envres.2022.113895.

Ramezanpour, B. and D. W. Mackowski. 2019. Direct prediction of bidirectional reflectance by dense particulate deposits, *J. Quant. Spectrosc. Radiat. Transfer*. 224:537-549. doi:10.1016/j.jqsrt.2018.12.012.

Rolph, G., A. Stein, and B. Stunder. 2017. Real-time Environmental Applications and Display sYstem: READY. *Environ. Model. Softw.* 95:210-228. https://doi.org/10.1016/j.envsoft.2017.06.025.

Samset, B. H. 2022. Aerosol absorption has an underappreciated role in historical precipitation change. *Commun. Earth Environ.* 3:242. doi:10.1038/s43247-022-00576-6.

Samset, B. H., C. W. Stjern, E. Andrews, R. A. Kahn, G. Myhre, M. Schulz, and G. L. Schuster. 2018. Aerosol absorption: Progress towards global and regional constraints. *Curr. Clim. Change Rep*. 4(2):65-83. doi:10.1007/s40641-018-0091-4.

Sand, M., B. H. Samset, G. Myhre, J. Gliß, S. E. Bauer, H. Bian, M. Chin, R. Checa-Garcia, P. Ginoux, Z. Kipling et al. 2021. Aerosol absorption in global models from AeroCom phase III. *Atmos. Chem. Phys.* 21:15929–15947. doi:10.5194/acp-21-15929-2021.

Scarnato, B. V., S. Vahidinia, D. T. Richard, and T. W. Kirchstetter. 2013. Effects of internal mixing and aggregate morphology on optical properties of black carbon using a discrete dipole approximation model. *Atmos. Chem. Phys.*13(10): 5089-5101. doi:10.5194/acp-13-5089-2013.

Scarnato, B. V., S. China, K. Nielsen, and C. Mazzoleni. 2015. Perturbations of the optical properties of mineral dust particles by mixing with black carbon: a numerical simulation study. *Atmos. Chem. Phys.* 15(12):6913-6928. doi:10.5194/acp-15-6913-2015.

Schuster, G. L., O. Dubovik, and A. Arola. 2016. Remote sensing of soot carbon–Part 1: Distinguishing different absorbing aerosol species. *Atmos. Chem. Phys.* 16(3):1565-1585. doi:10.5194/acp-16-1565-2016.

Slowik, J. G., Cross, E. S., Han, J. H., Davidovits, P., Onasch, T. B., Jayne, J. T., Williams, L. R., Manjula R. Canagaratna, M. R., Worsnop, D. R., Chakrabarty, R. K. et al. 2007. An inter-comparison of instruments measuring black carbon content of soot particles. *Aerosol Sci. Technol.* 41(3):295-314. doi:10.1080/02786820701197078.

Stagg, B. J. and T. T. Charalampopoulos. 1993. Refractive indices of pyrolytic graphite, amorphous carbon, and flame soot in the temperature range 25 to 600 C. *Combust. Flame.* 94(4):381-396. doi:10.1016/0010-2180(93)90121-I.

Stein, A. F., R. R. Draxler, G. D. Rolph, B. J. B. Stunder, M. D. Cohen, and F. Ngan. 2015. NOAA's HYSPLIT atmospheric transport and dispersion modeling system. *Bull. Am. Meteor. Soc.* 96:2059-2077. doi:10.1175/BAMS-D-14-00110.1.

Stier, P., J. H. Seinfeld, S. Kinne, and O. Boucher. 2007. Aerosol absorption and radiative forcing. *Atmos. Chem. Phys.* 7(19):5237-5261. doi:10.5194/acp-7-5237-2007.

Wang, Y., F. Liu, C. He, L. Bi, T. Cheng, Z. Wang, H. Zhang, X. Zhang, Z. Shi, and W. Li. 2017. Fractal dimensions and mixing structures of soot particles during atmospheric processing. *Environ. Sci. Technol. Lett.* 4(11):487-493. doi:10.1021/acs.estlett.7b00418.

Wu, Y., T. Cheng, L. Zheng, and H. Chen. 2015. A study of optical properties of soot aggregates composed of poly-disperse monomers using the superposition T-matrix method. *Aerosol Sci. Technol.* 49(10):941-949. doi:10.1080/02786826.2015.1083938.

Wu, Y., T. Cheng, D. Liu, J. D. Allan, L. Zheng, and H. Chen. 2018. Light absorption enhancement of black carbon aerosol constrained by particle morphology. *Environ. Sci. Technol.* 52(12):6912-6919. doi:10.1021/acs.est.8b00636.

Yoshida, A., N. Moteki, and K. Adachi. 2022. Identification and particle sizing of submicron mineral dust by using complex forward-scattering amplitude data. *Aerosol Sci. Technol.* 56(7):609–622. doi:10.1080/02786826.2022.2057839.

Yu, F. G. Luo, and X. Ma. 2012. Regional and global modeling of aerosol optical properties with a size, composition, and mixing state resolved particle microphysics model. *Atmos. Chem. Phys.* 12(13):5719-5736. doi:10.5194/acp-12-5719-2012.

Zaveri, R. A., J. C. Barnard, R. C. Easter, N. Riemer, and M. West. 2010. Particle-resolved simulation of aerosol size, composition, mixing state, and the associated optical and cloud condensation nuclei activation properties in an evolving urban plume. *J. Geophys. Res. Atmos.* 115:D17210. doi:10.1029/2009JD013616.

Table 1. List of the publications using the BB06-h, BB06-l, and CC90 for BC refractive index.

Category	Authors and Year	Research focus	BC refractive index values used/refereed
Light-scattering simulation	Moosmüller et al. (2009)	Review of aerosol light absorption and its measurement techniques	BB06-h
	Kahnert and Devasthale (2011)	Spectral optical properties of pure BC aggregates	CC90
	Cheng et al. (2013)	Spectral optical properties of BC-containing particles	CC90
	Scarnato et al. (2013)	Mass absorption cross-section of NaCl-BC mixture	BB06-h
	Scarnato et al. (2015)	Spectral optical properties of a dust-BC mixture	CC90
	Wu et al. (2015)	Effect of monomer polydispersity of BC aggregates on its mass absorption cross-section	BB06-h
	Wu et al. (2018)	Morphological effects of absorption enhancement	CC90
	Beeler and Chakrabarty (2022)	Parameterization of mass absorption cross-section of BC-containing particles	BB06-h
Aerosol remote sensing	Koike et al. (2014)	Interpretation of aerosol absorption optical depth from in-situ aircraft data	BB06-h, Average of BB06-h and -l
	Schuster et al. (2016)	Distinguishing different absorbing aerosol species	BB06-h, BB06-l
	Li et al. (2019)	Retrieval of aerosol components	BB06-h, BB06-l
Aerosol's treatment in climate model	Stier et al. (2007)	Global distribution of aerosol absorption, climate model	BB06-h, BB06-l
	Zaveri et al. (2010)	Modeling aerosol's microphysical properties, particle-resolved aerosol box model	Midpoint of BB06-h and -l
	Yu et al. (2012)	Aerosol microphysics module for climate models	Average of BB06-h and -l
	Brown et al. (2021)	Intercomparison of biomass aerosol absorption among climate models	BB06-h, BB06-l, Average of BB06-h and -l

Table 2. List of the particle shape models and their parameters $(r_{\mathrm{v}}, m_{\mathrm{r}}, m_{\mathrm{i}}, \theta_{\mathrm{s}})$.

Shape model	Morphology	Model constants	Number of monomers	Volume equivalent radius r_{v}	Real part of refractive index m_{r}	Imag. part of refractive index m_{i}	Shape parameter θ_s
AGGREGATE	A fractal-like aggregate of spherical monomers	Monomer radius r_{pp} = 0.030 μm, Fractal prefactor k_{f} = 1.0	N_{pp} = $2^2, 2^3, \ldots, 2^{14}$	0.048–0.76 μm, 13 grid points in log space	1.4–3.3, 20 grid points in linear space	0.0–1.5, 16 grid points in linear space	Fractal dimension 2.0–2.5 6 grid points in linear space
SPHPACK	Randomly positioned non-overlapping spherical monomers within a spherical volume	Monomer radius r_{pp} = 0.030 μm					Packing density 0.05–0.3 6 grid points in linear space

630

Table 3. List of the laboratory test samples

Sample name	Chemical composition	Supplier and product number	Morphology of individual particles from TEM images
Fullerene Soot	Synthetic BC powder consisting of aggregates of ns-soot nanoparticles	Alfa Aesar, Inc. Stock# 40971, Lot#FS12S011	Compact aggregate of near-spherical nanoparticles with monomer diameter ~20−50 nm. Essentially all the attached monomer pairs are sintered.
Vehicle Exhaust Particulates	Reference material of vehicle exhaust particles. BC mass fraction of this power was estimated to be ~80% (Honda 2021)	National Institute of Environmental Studies, Japan. Certified Reference Material No.8: Vehicle Exhaust Particulates.	Compact aggregate of near-spherical nanoparticles with monomer diameter ~10−40 nm. Most of the attached monomer pairs are weakly sintered.
Hematite-KJ	Synthetic hematite powder consisting of aggregate of α-Fe_2O_3 nanoparticles	Kojundo Chemical Laboratory Co. Ltd., FEO14PB, 99.9% purity, c.a. 0.3 μm	Compact aggregate of nonspherical nanoparticles with monomer maximum dimension < ~100 nm. Essentially all the attached monomer pairs are strongly sintered.
Hematite-TD	Synthetic hematite powder consisting of aggregate of α-Fe_2O_3 nanoparticles	Toda Kogyo Co. Lot# 180611 Specific surface area = 10.5 m^2g^{-1}	Compact aggregate of near-spherical nanoparticles with monomer diameter ~30−100 nm. Most of the attached monomer pairs are not sintered.

635

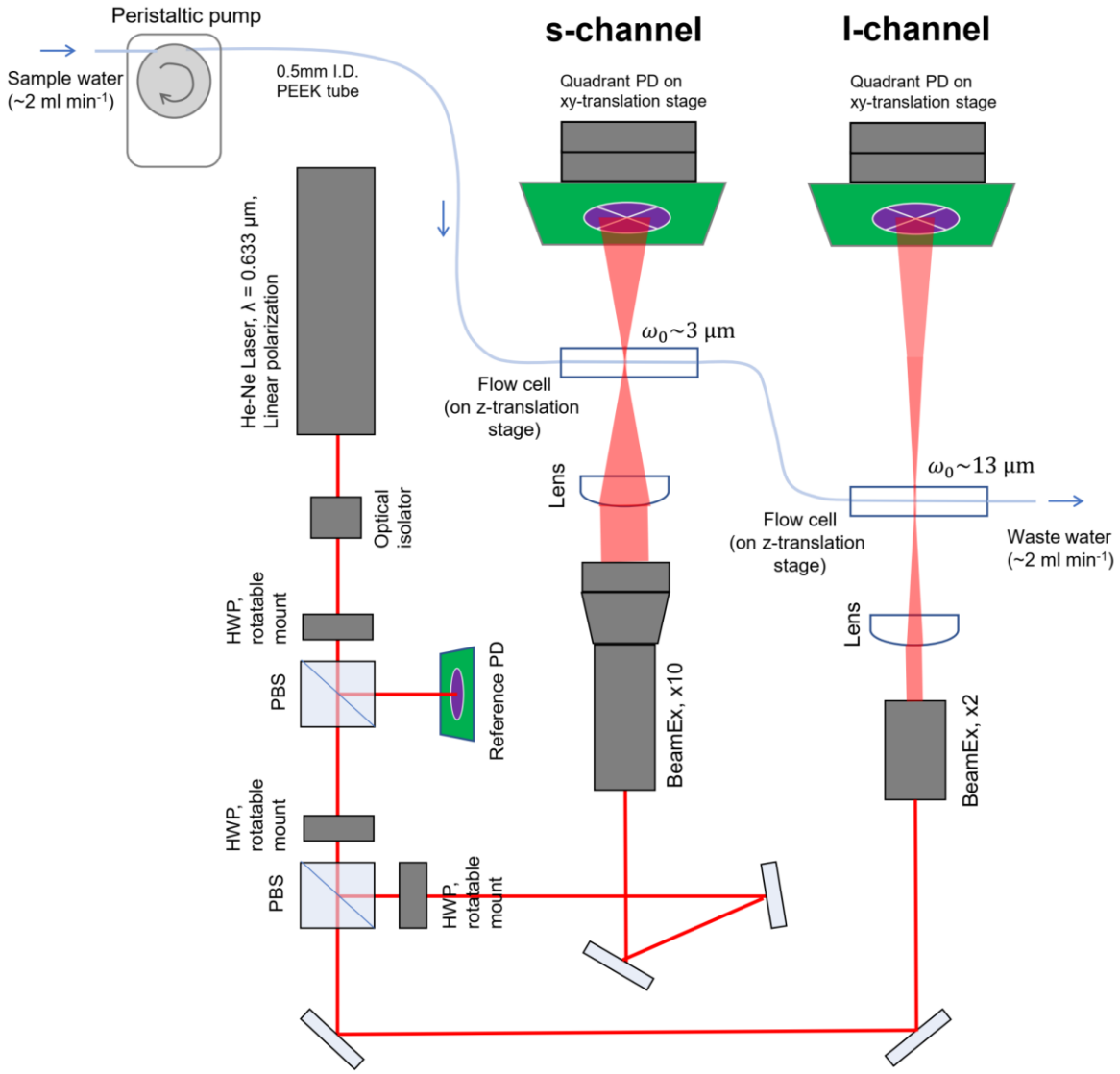

FIG. 1. Schematic diagram of the complex amplitude sensor for waterborne particles. A linearly polarized 2 mW He-Ne laser with λ = 0.633 μm was used for generating high-wavefront quality Gaussian laser beam. An optical isolator was used to prevent laser instability due to back reflections. Each pair of rotatable Harf-wave plate (HWP) with a polarization beam splitter (PBS) was used to split the beam with a controlled power ratio. The beam optics in the s- and l-channels are configured to quantify the complex forward-scattering amplitude of the sub- and super-micron particle size range, respectively. Other details of the instrument and the procedure of signal processing were described in Moteki (2021).

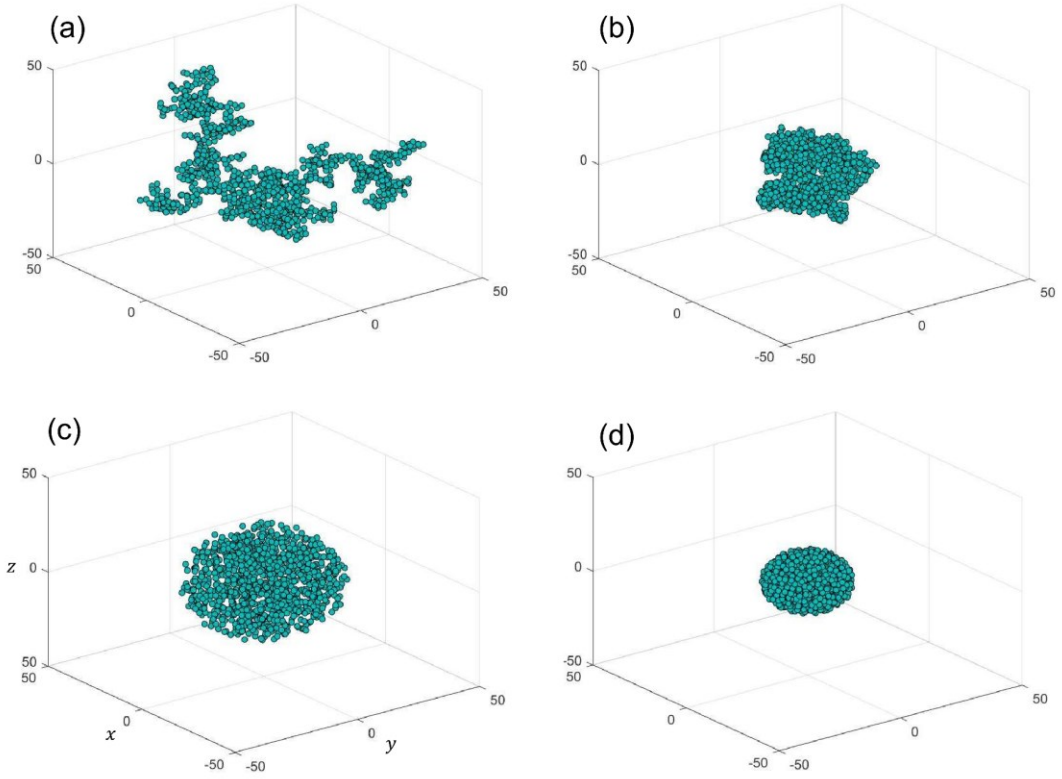

FIG. 2. Examples of the geometric arrangement of spherical monomers in the AGGREGATE and SPHPACK models. (a) AGGREGATE with fractal dimension 2.0, (b) AGGREGATE with fractal dimension 2.5, (c) SPHPACK with packing density 0.05, (d) SPHPACK with packing density 0.30. The number of monomers N_{pp} is 1024 in each example. The length unit of each Cartesian coordinate is the monomer radius.

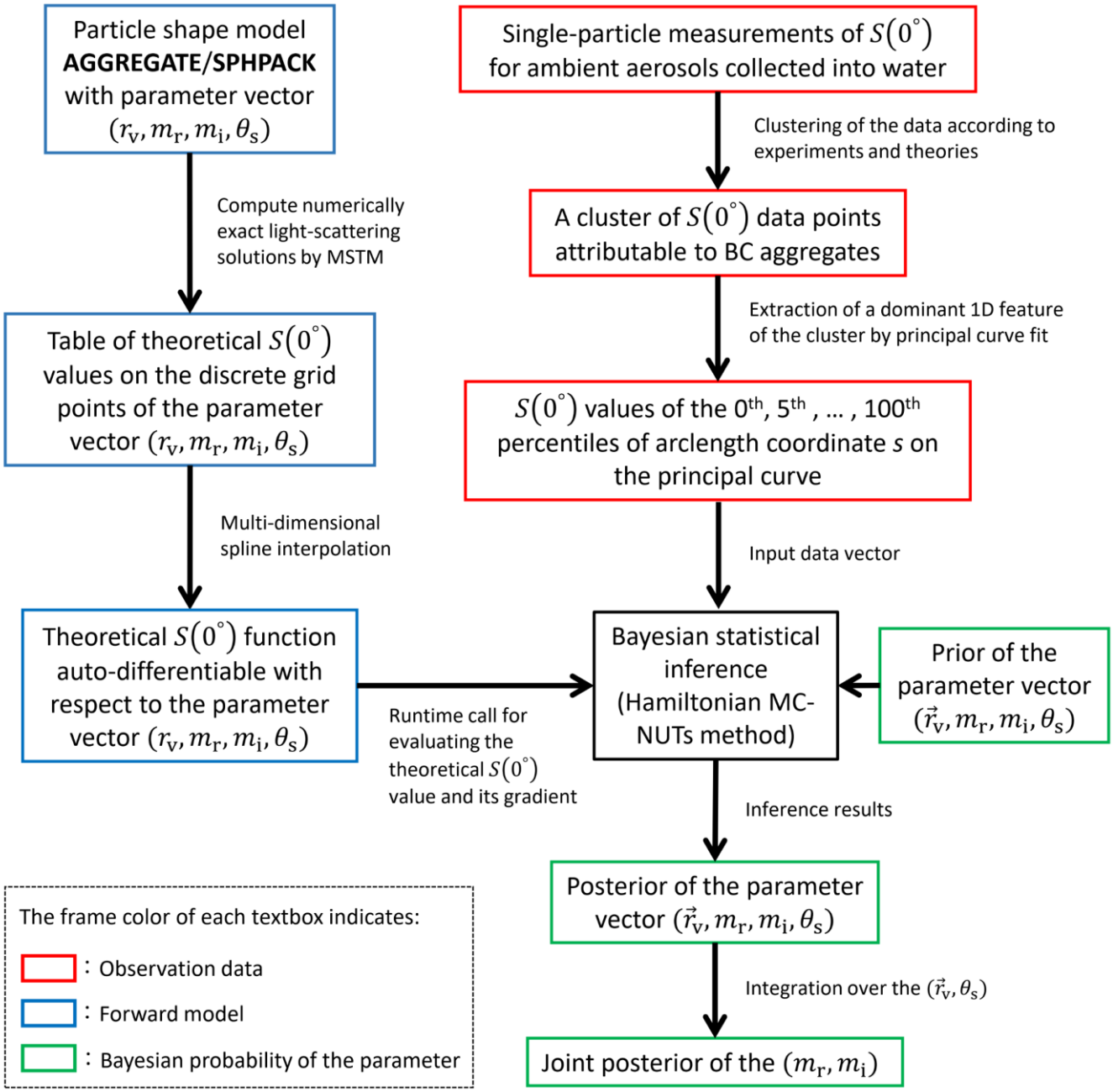

FIG. 3. Flow chart of the computational and data processing procedure in our method for constraining the refractive index of ambient BC from the complex forward-scattering amplitude measurements. The frame color shows either of data, forward model, or Bayesian probability as illustrated in the lower-left part of the Figure.

660

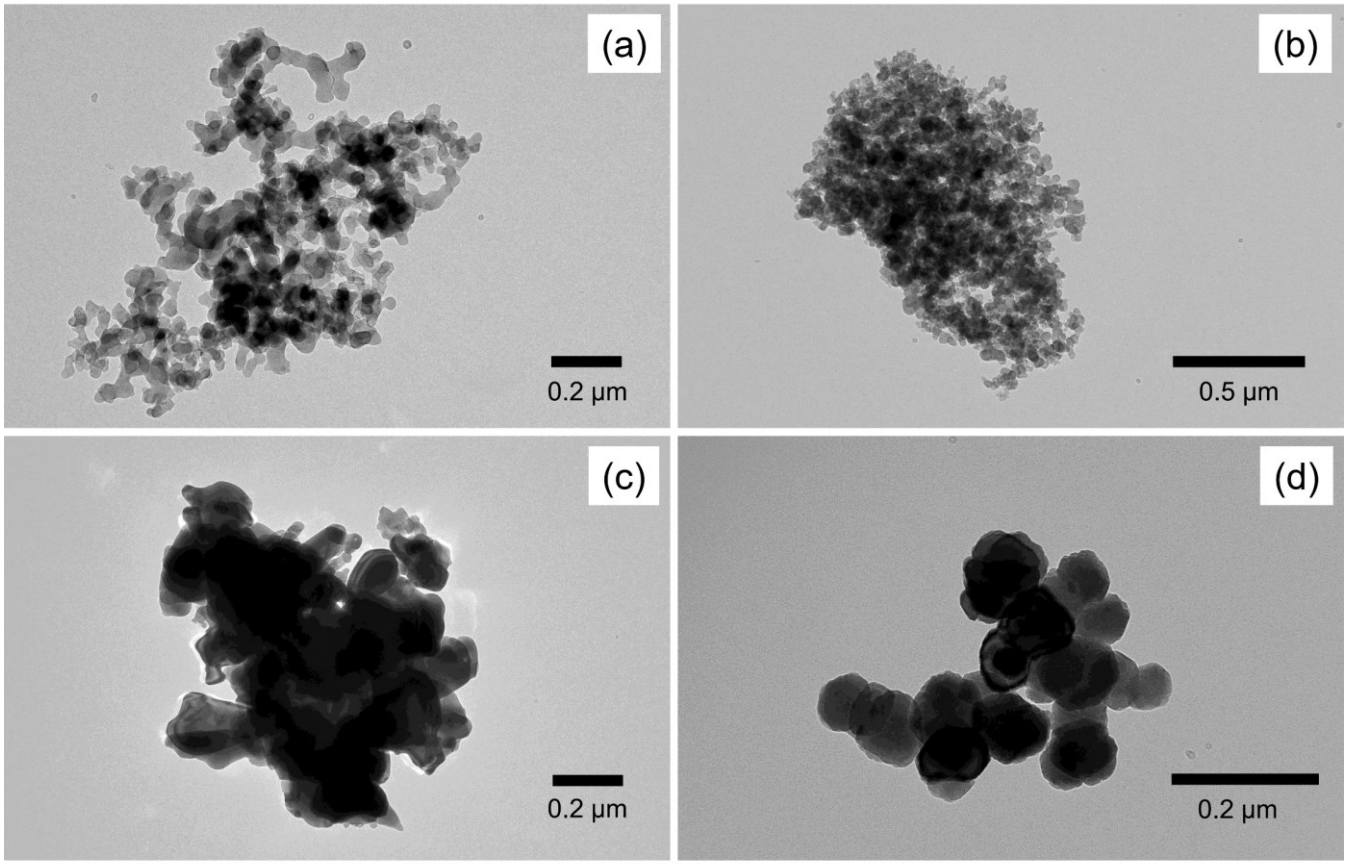

FIG. 4. Typical examples of transmission electron microscope (TEM) images of laboratory powder samples. (a) Fullerene soot, (b) BC aggregate in the Vehicle exhaust particulates, (c) Hematite-KJ, and (d) Hematite-TD. The TEM images were obtained using a 120-kV
665 TEM (JEM-1400, JEOL).

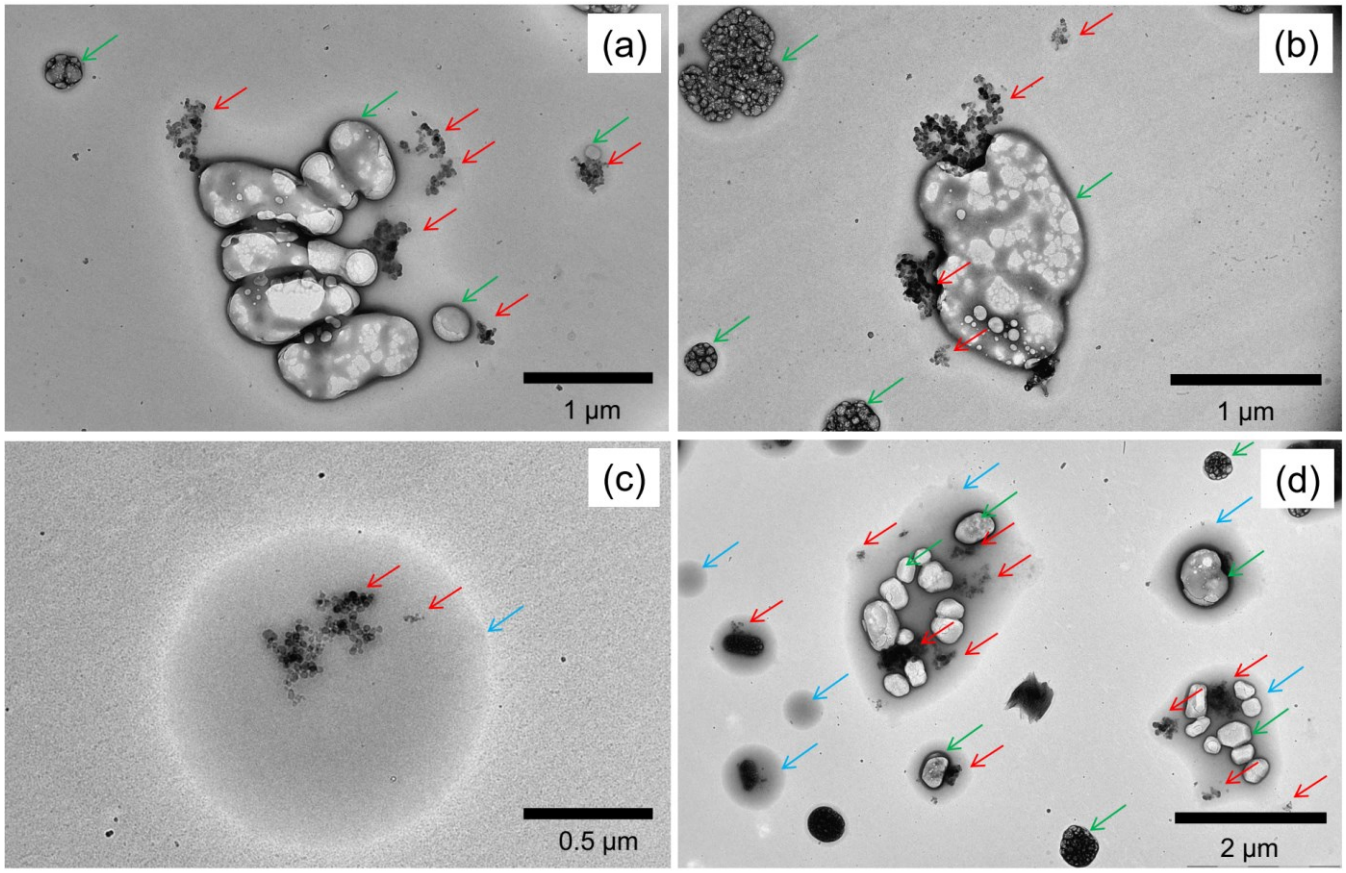

FIG. 5. Typical examples of transmission electron microscope (TEM) images of ambient aerosols collected by an aerosol-impactor sampler installed on the research vessel SHINSEI MARU. Each panel shows samples collected around 12:00 local time on (a) July 27th, (b) July 28th, (c) July 30th, and (d) August 1st. Red arrows indicate individual BC aggregates, most of which were mixed with sulfate (green arrows) and/or organics (light blue arrows). The TEM images were obtained using a 120-kV TEM (JEM-1400, JEOL).

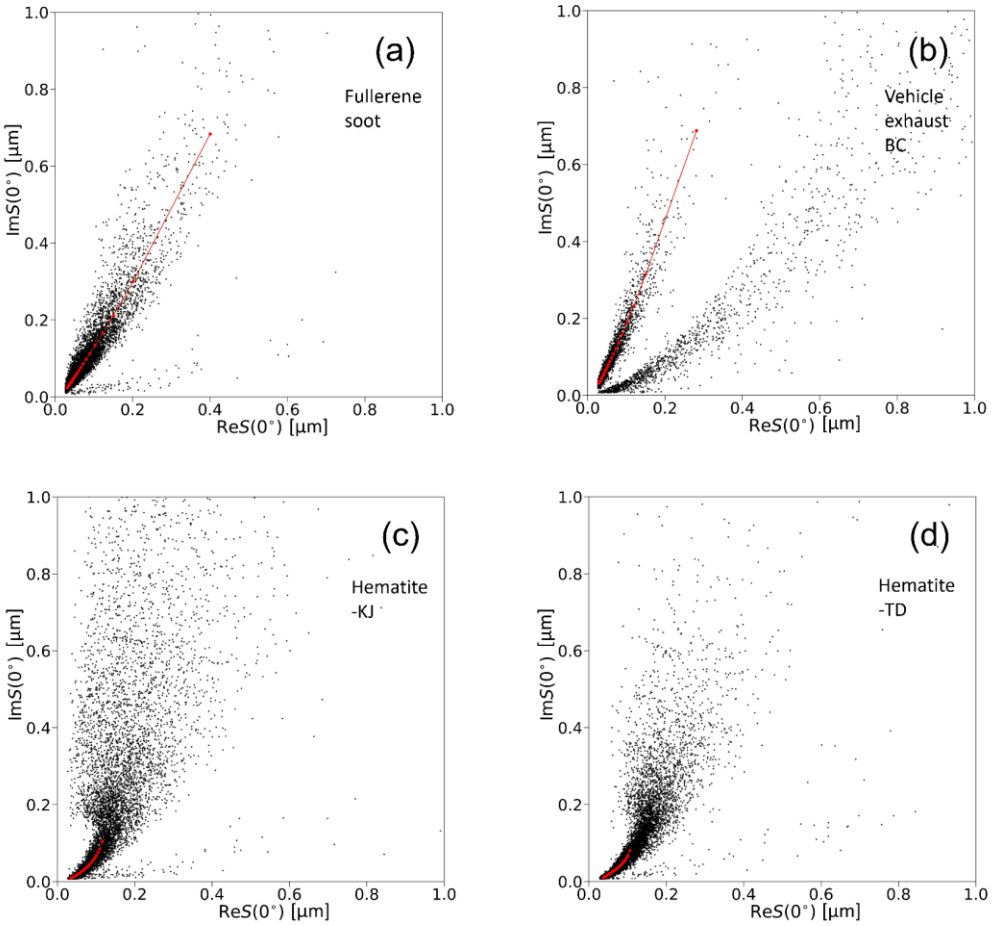

FIG. 6. Scatterplot of the complex forward-scattering amplitude obtained for each of the laboratory powder samples suspended in water. Black dots show raw single particle $\boldsymbol{S}(\mathbf{0}^{\circ})$ data. The red-filled circles show the 0^{th}, 5^{th}, …, and 100^{th} percentiles of the arclength coordinate of the principal curve. These 21 data points were used as the observation data vector for Bayesian inference. The red circles are concentrated in proportion to the local density of raw data points.

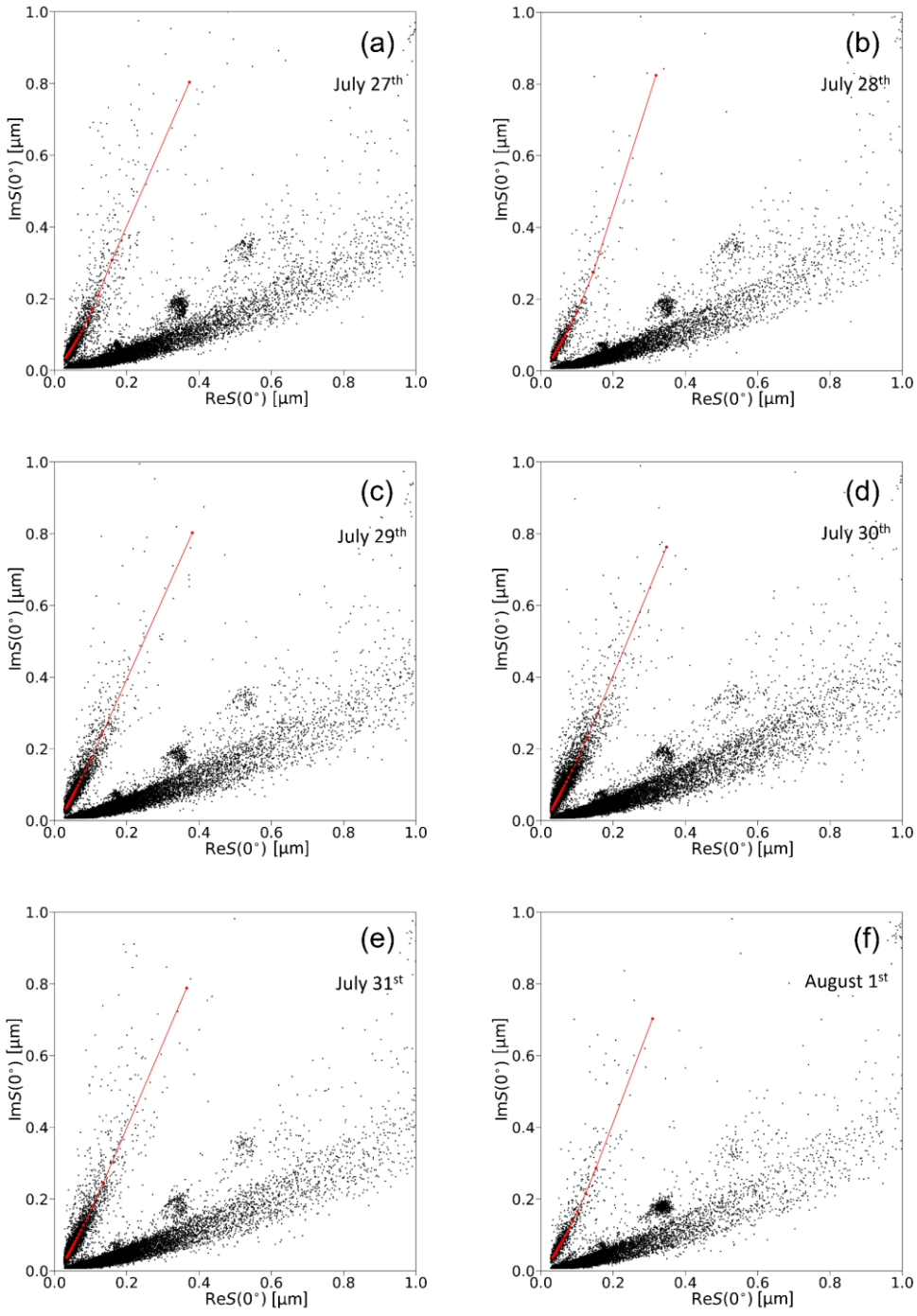

FIG. 7. Same plots as Figure 6 but for ambient water-insoluble aerosols sampled on each of the 6 observation days. Principal curve fit was applied to the linear-shape cluster of data points with $\mathbf{Im}\boldsymbol{S}(\mathbf{0}^{\circ})/\mathbf{Re}\boldsymbol{S}(\mathbf{0}^{\circ})$ > ~1, which is attributable to BC aggregates.

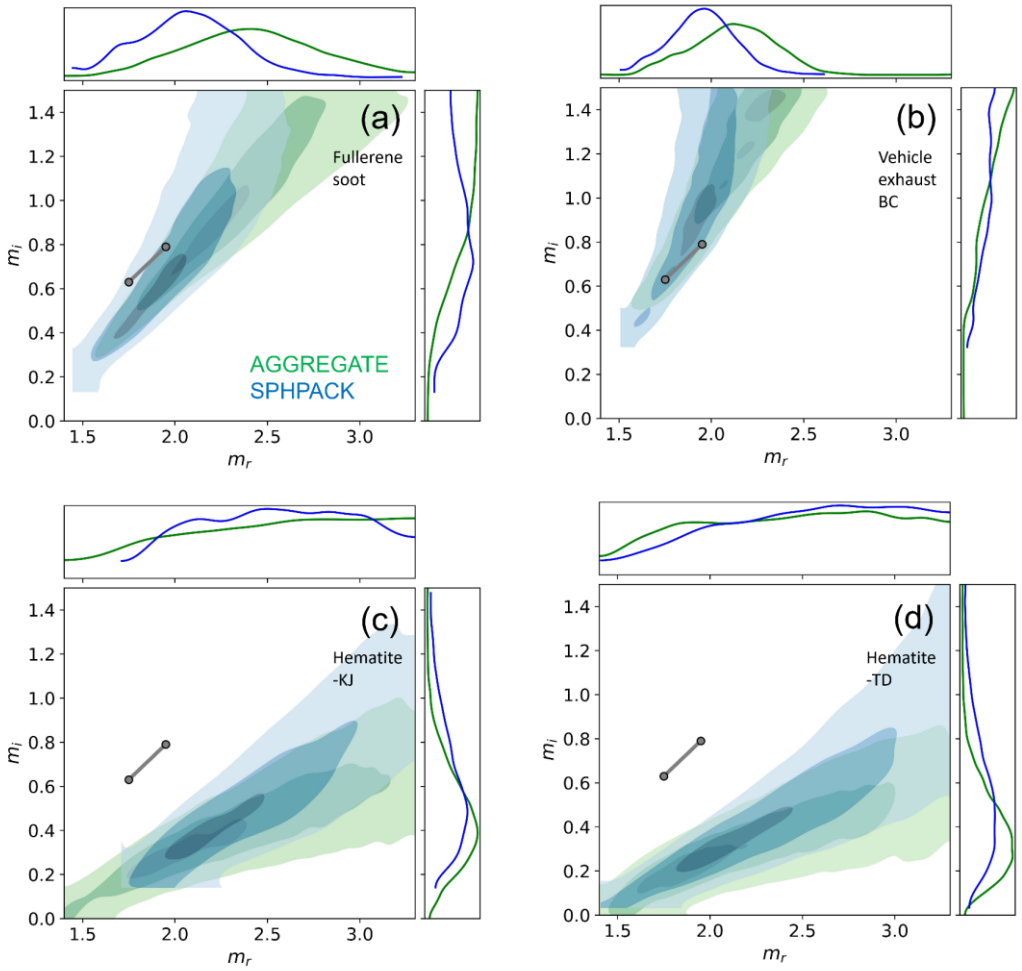

FIG. 8. Posterior of real and imaginary parts of complex refractive index ($\boldsymbol{m_r}, \boldsymbol{m_i}$) for each laboratory sample derived from the data shown in Figure 6. (a) Fullerene soot, (b) Vehicle exhaust BC, (c) Hematite-KJ, (d) Hematite-TD. The three-level contour shows the 90%, 50%, and 10% highest density credibility regions for each of the AGGREGATE (green) and SPHPACK (blue) models. Marginalized density distributions of $\boldsymbol{m_r}$ and $\boldsymbol{m_i}$ are also shown along horizontal and vertical axes, respectively. In each panel, the BB06-l and -h values were also shown by gray-filled circles for comparison. In panels (a) and (b), the SPHPACK is more realistic shape model than the AGGREGATE for the reasons explained in the main text.

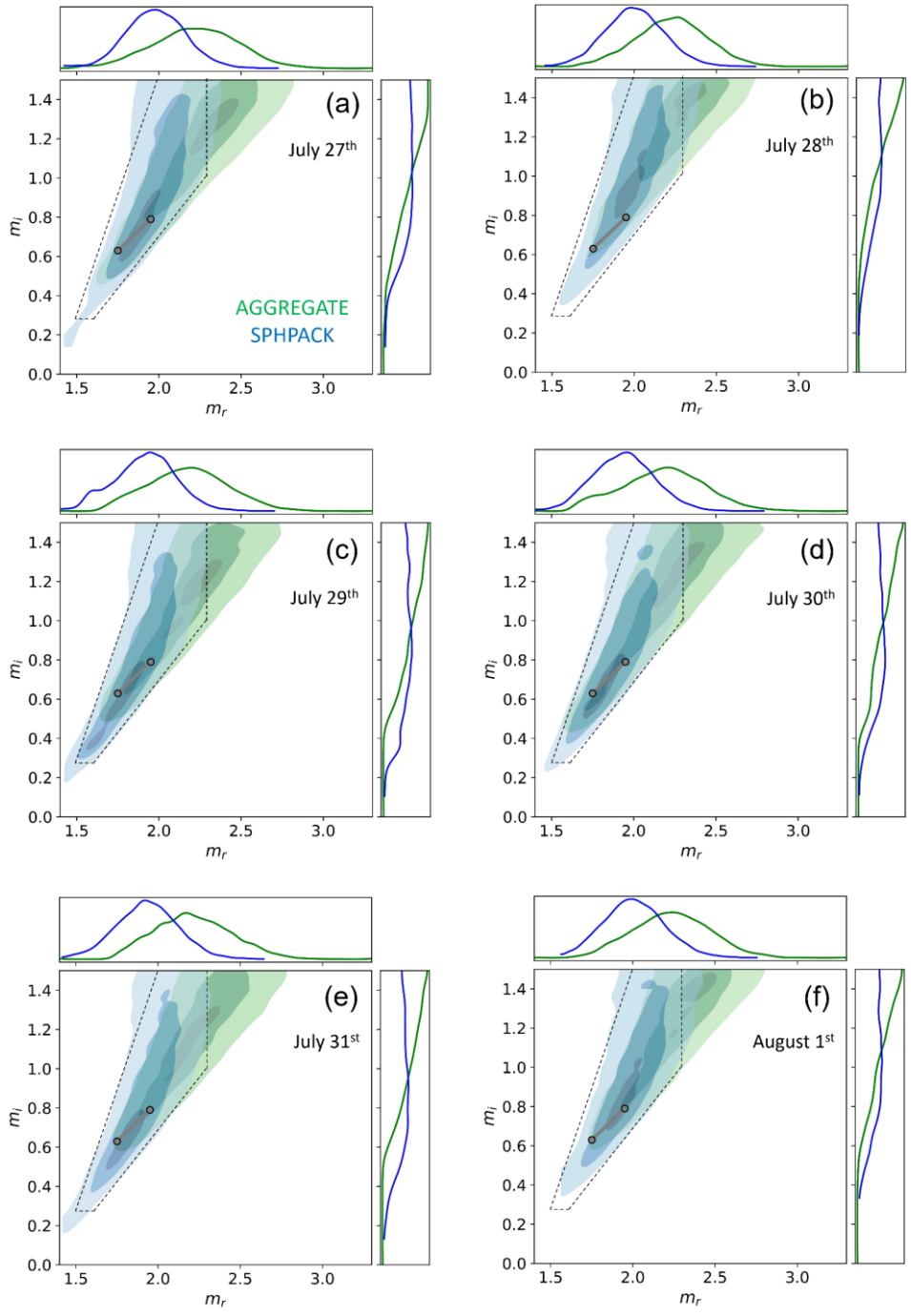

695

FIG. 9. Same plot as Figure 8 but for ambient BC results derived from the data shown in Figure 7. In each panel, the BB06-l and -h values were also shown by gray-filled circles for comparison. The dashed lines indicate the borderlines of our suggested plausible $(\boldsymbol{m_r}, \boldsymbol{m_i})$ domain for ambient BC refractive index. The SPHPACK is more realistic shape model than the AGGREGATE for the reasons explained in the main text.

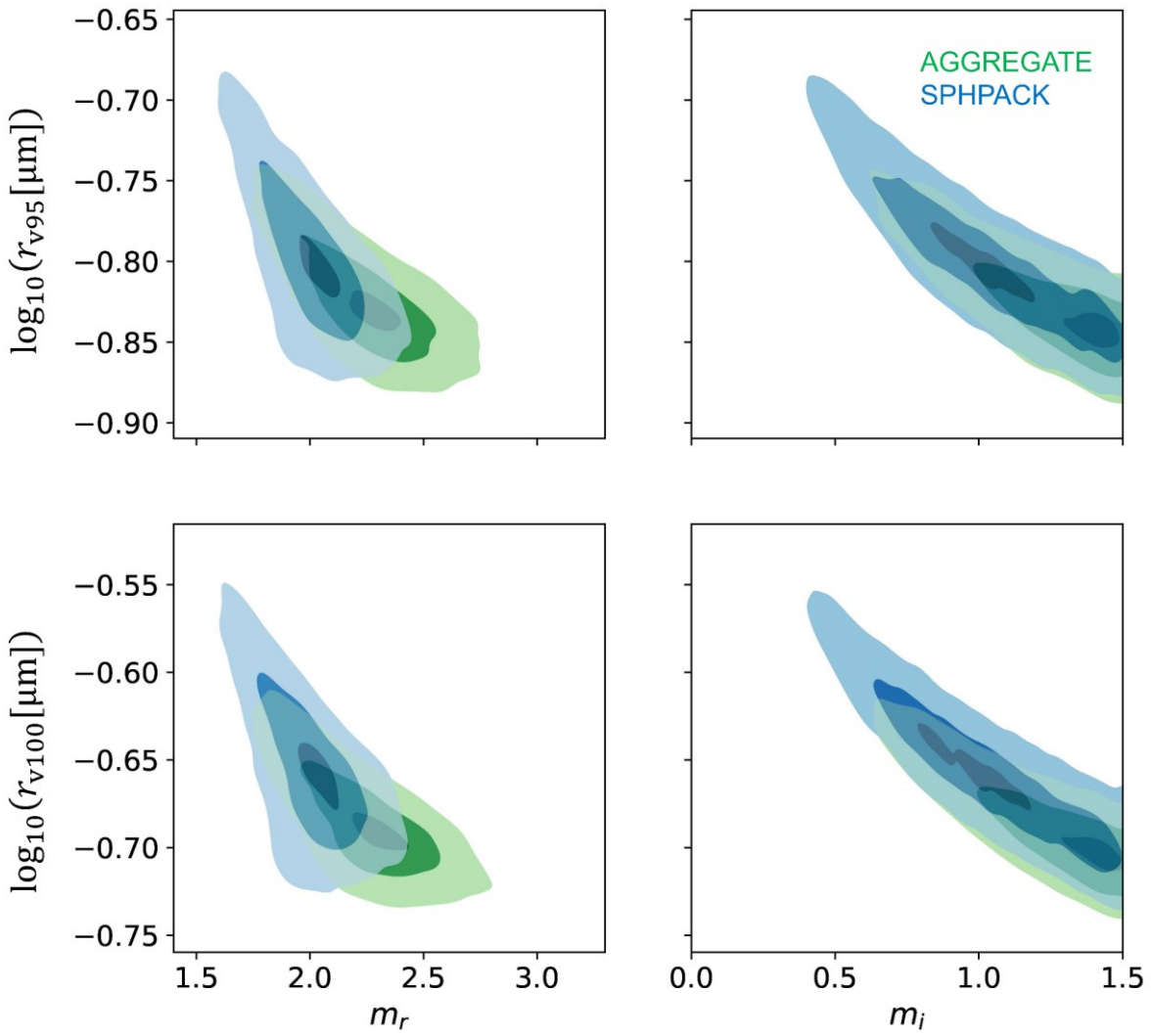

FIG. 10. Joint density plots of the posteriors of real and imaginary parts of refractive index, m_r, m_i, and the two volume-equivalent radii corresponding to the 95th and 100th percentiles of arclength coordinate of the principal curve, r_{v95}, r_{v100} for ambient BC sampled on August 1st. The three-level contour shows the 90%, 50%, and 10% highest density credibility regions in each of the AGGREGATE (green) and SPHPACK (blue) models. The SPHPACK is more realistic shape model than the AGGREGATE for the reasons explained in the main text.

Supplement of

Constraining the complex refractive index of ambient black carbon particles from their observed distribution of the complex forward-scattering amplitude

Nobuhiro Moteki et al.
Correspondence to: Nobuhiro Moteki (nobuhiro.moteki@gmail.com)

FIG. S1. Photo of the research vessel SHINSEI-MARU cruising the north-western Pacific on July 21st, 2022, during the observation campaign. (©Makoto Koike). The SHINSEI-MARU is operated by the Japan Agency for Marine-Earth Science and Technologies (JAMSTEC), Japan.

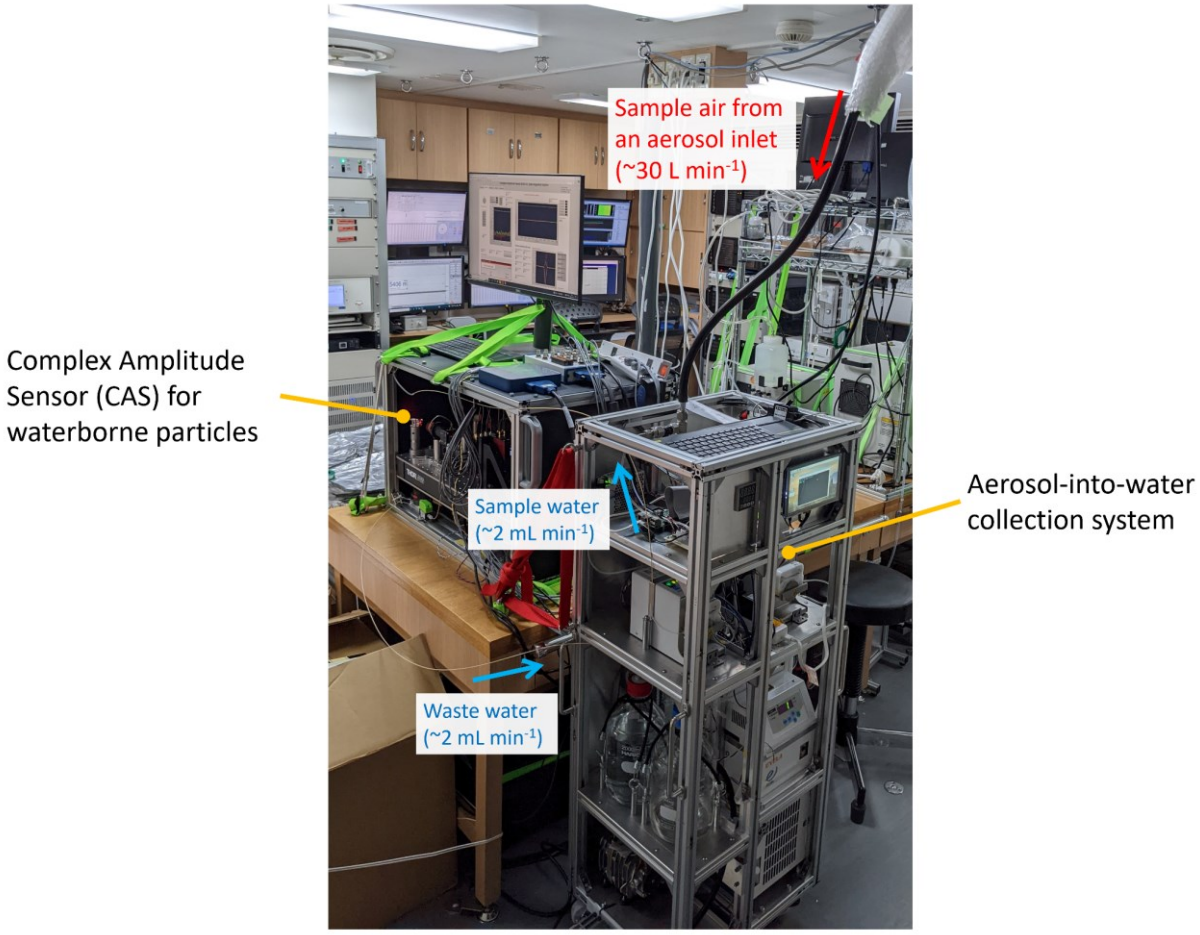

FIG. S2. Photo of the complex amplitude sensor connected to the aerosol-into-water collection system, installed in a cabin of research vessel SHINSEI MARU during the observation campaign.

735

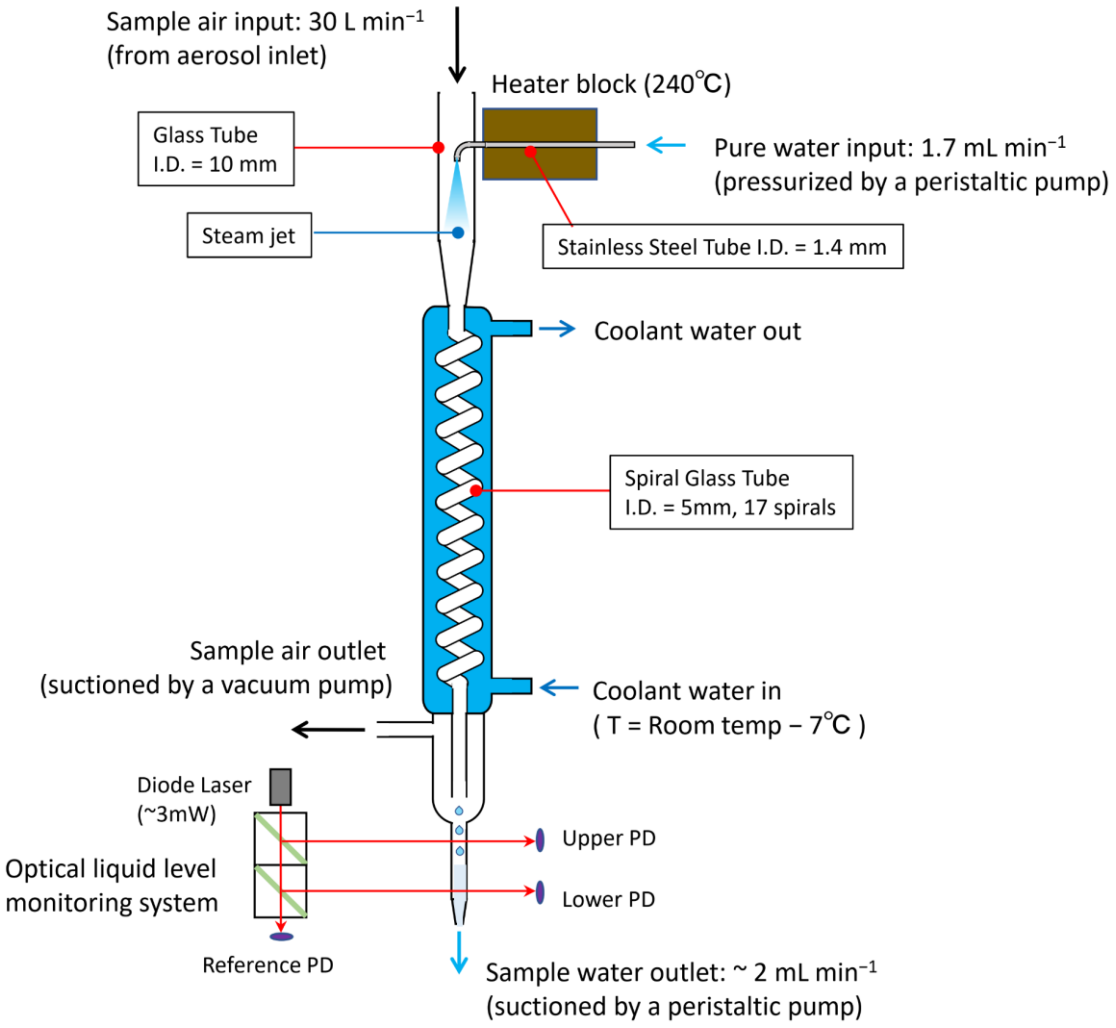

FIG. S3. Schematic diagram of the aerosol-into-water collection system for water-insoluble particles. The sample airflow (30 L min^{-1}) is mixed with a steam jet (generated from 1.7 mL min^{-1} pure water) under a turbulent condition (Reynolds number ~4000). The supersaturated sample air flows through a glass-made spiral condenser tube maintained at ~7°C cooler than the sample flow temperature. The aerosol particles activated to cloud droplets deposit the inner wall of the spiral tube by the outward centrifugal force experienced in the spiral flow. The whole inner surface of the glass tubes in the collection system was coated with a pollution prevention chemical Fluoro Surf® (Product code FG-5080S135-0.1; FluoroTechnology Co. ltd.). The level of the condensed water in the outlet buffer tube is monitored by a homemade optical liquid level sensor. The suctioned flow rate of sample water (~2 mL min^{-1}) is servo-controlled to maintain the liquid level to be within an optimal range.

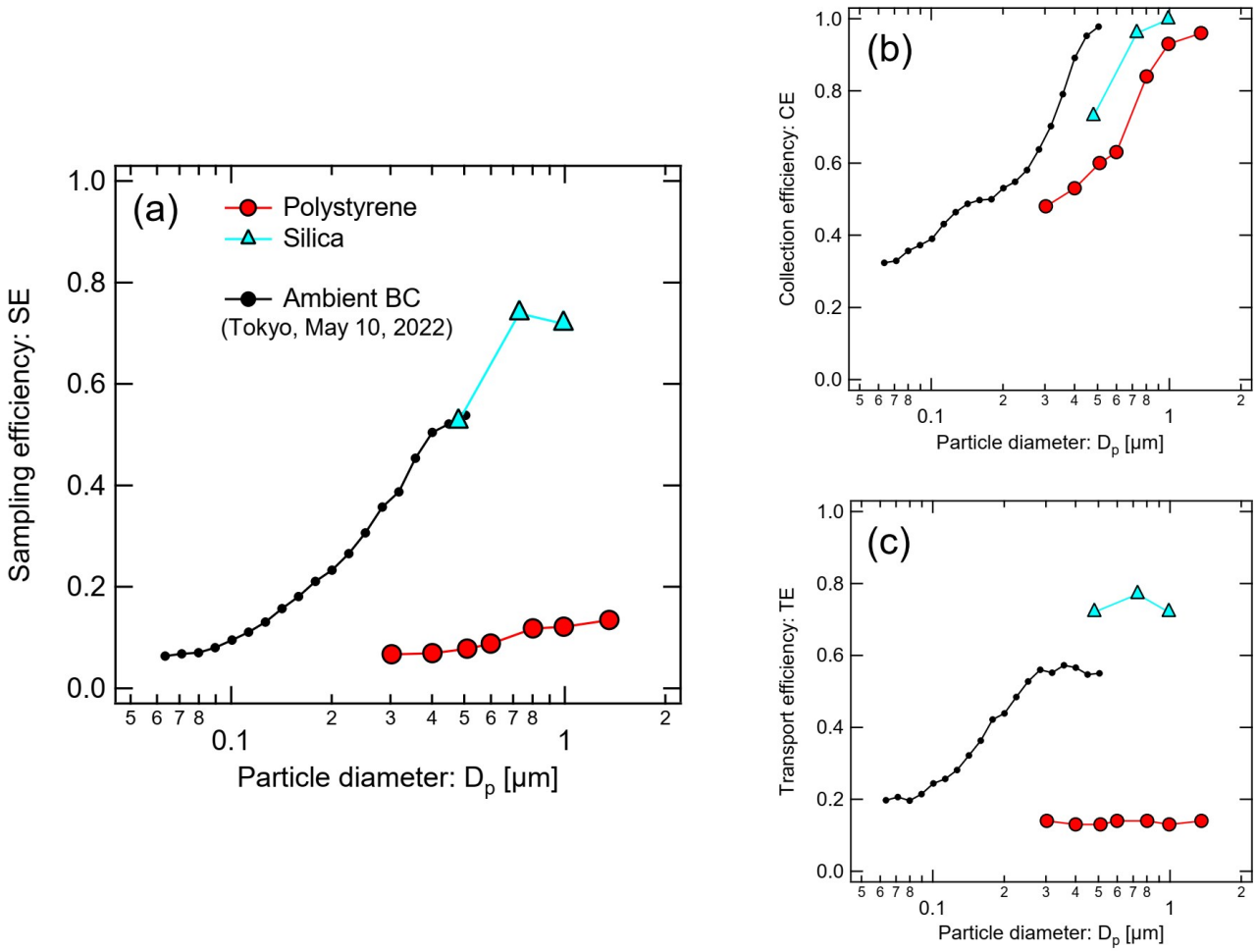

FIG. S4. Laboratory test results of the aerosol-into-water collection system using three different particulate materials (Polystyrene, Silica, and ambient BC). (a) Sampling efficiency (SE) is the number fraction of aerosol particles collected in water and transported to the outlet buffer tube. (b) Collection efficiency (CE) is the number fraction of aerosol particles removed from the sampled airflow. (c) Transport efficiency (TE) is the number fraction of removed aerosol particles transported to the outlet buffer tube. SE=CE×TE. The particle-size dependence of CE would be due to the size dependence of the critical supersaturation and spatiotemporal inhomogeneity of supersaturation due to insufficient mixing of steam jet and sample airflow. The strong material dependence of TE would be due to the difference in the zeta potential of waterborne particles that determine the tendency of adsorption of waterborne particles on the inner wall of the spiral tube. Commercial-size standard microspheres (ThermoFisher Scientific) were used for polystyrene and silica samples. The number concentrations of each size standard particulate sample in air and water were respectively measured using an optical particle counter (SPS30, Sensirion) without and with a Marin-5 nebulizer (Teledyne CETAC Technologies). For ambient BC, size-resolved number concentrations in air and water are respectively measured using the single-particle soot photometer (SP2; Droplet Measurement Technologies) without and with a Marin-5 nebulizer. Ambient BC sampling was performed on the Hongo campus of the University of Tokyo on May 10, 2022.

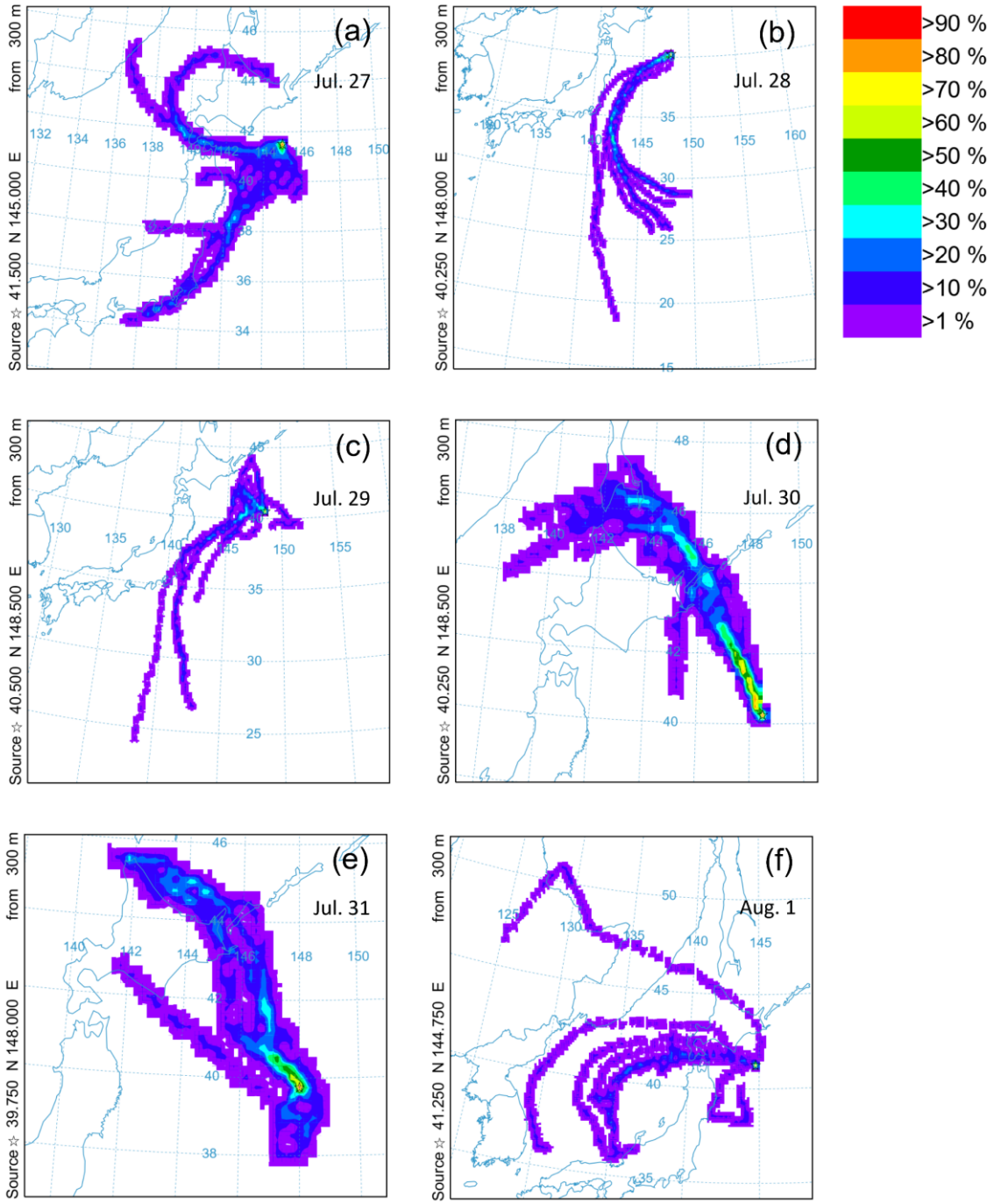

770 **FIG. S5.** Frequency map of backward trajectories of air parcels observed by the RV SHINSEI MARU on each of the 6 days. The frequency on each 0.25°×0.25° horizontal grid was derived from the 72 hours backward trajectories in 3 hours intervals (8 trajectories per day) starting from the location of the RV SHINSEI MARU. The calculations and visualizations were performed by using the NOAA HYSPLIT-WEB system.

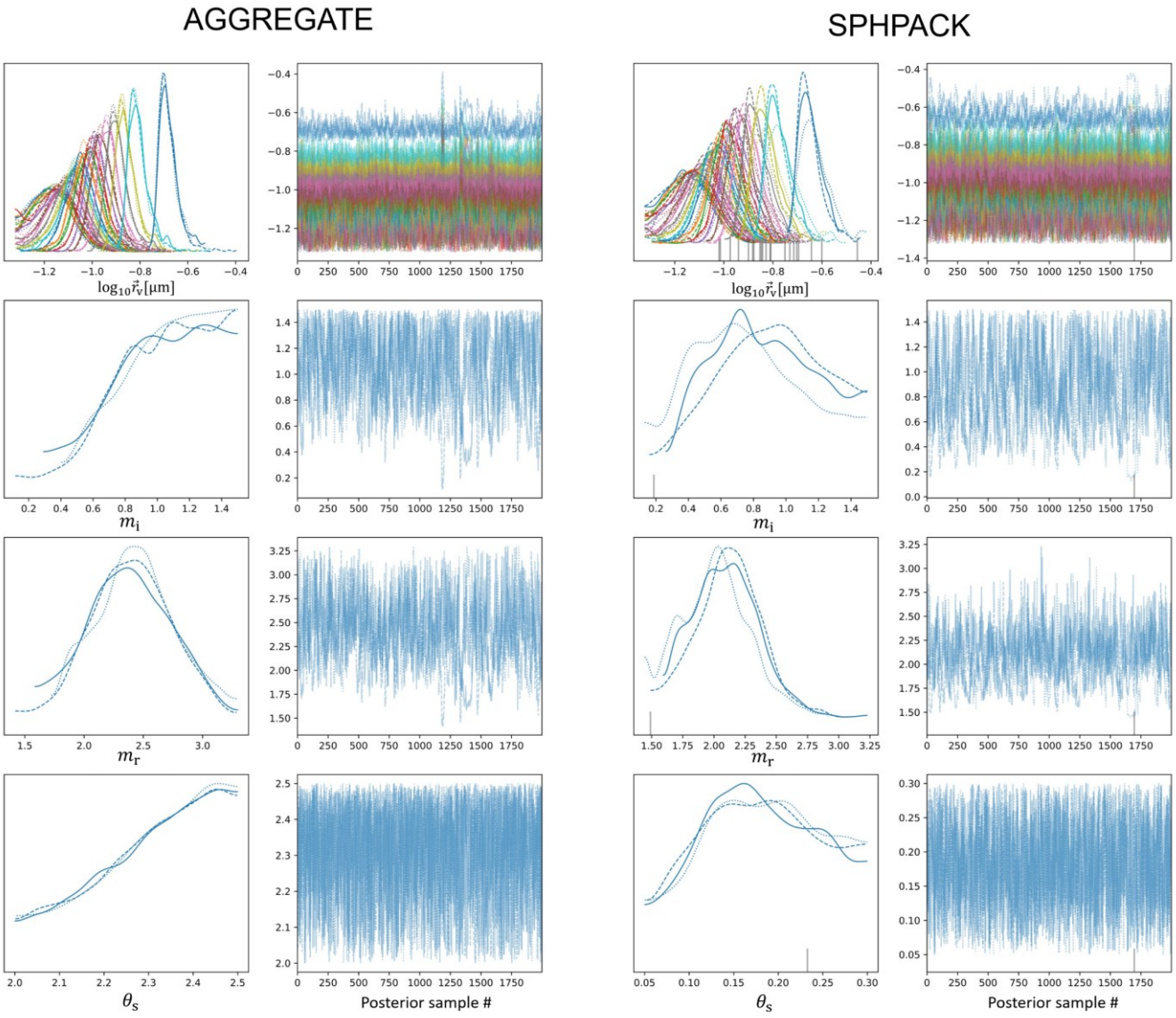

FIG. S6. Histogram and trace plot of 2000 posterior samples for each element of the parameter vector $(\vec{r}_v, m_r, m_i, \theta_s)$ obtained by the Hamiltonian MC-NUTs using the $S(0^\circ)$ data of Fullerene soot. The left and right columns show the results assuming the AGGREGATE and SPHPACK shape models, respectively. The different line styles indicate the independent chains run in parallel. The shape parameter θ_s represents the fractal dimension for the AGGREGATE model and the packing density for the SPHPACK model. The length unit of $\vec{r}_v$ is μm.

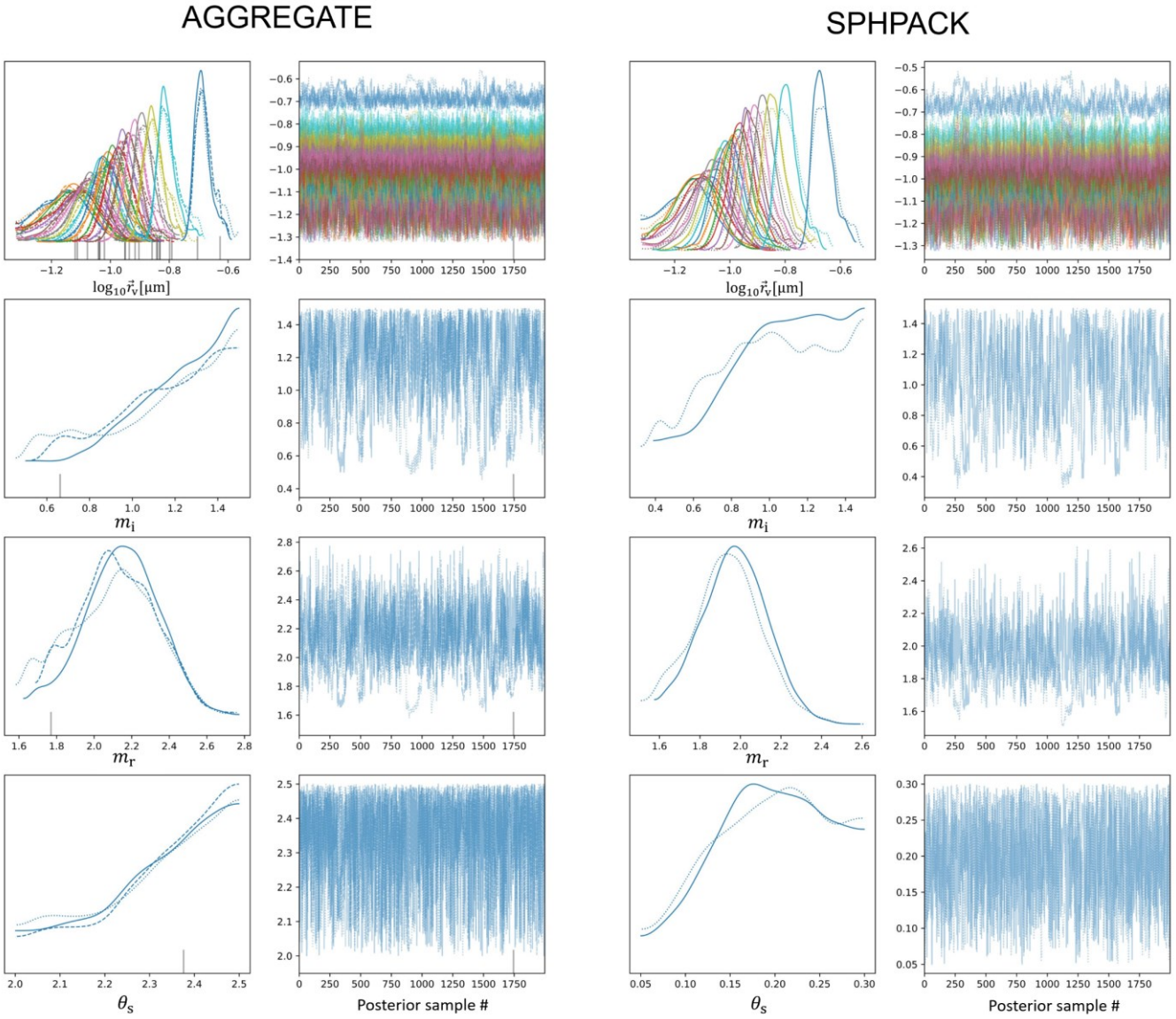

FIG. S7. Same as Figure S6 for Vehicle exhaust BC.

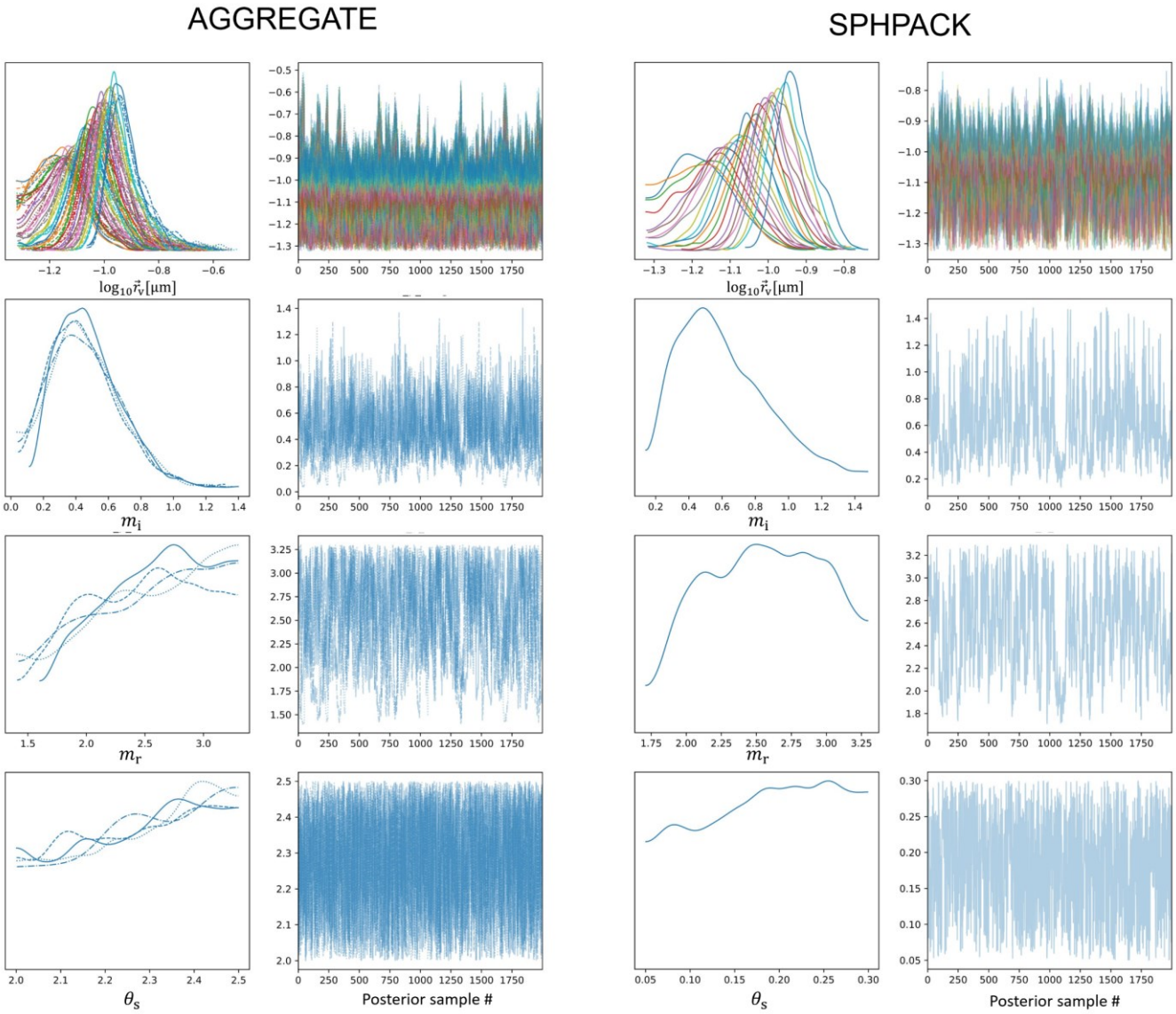

FIG. S8. Same as Figure S6 for Hematite-KJ.

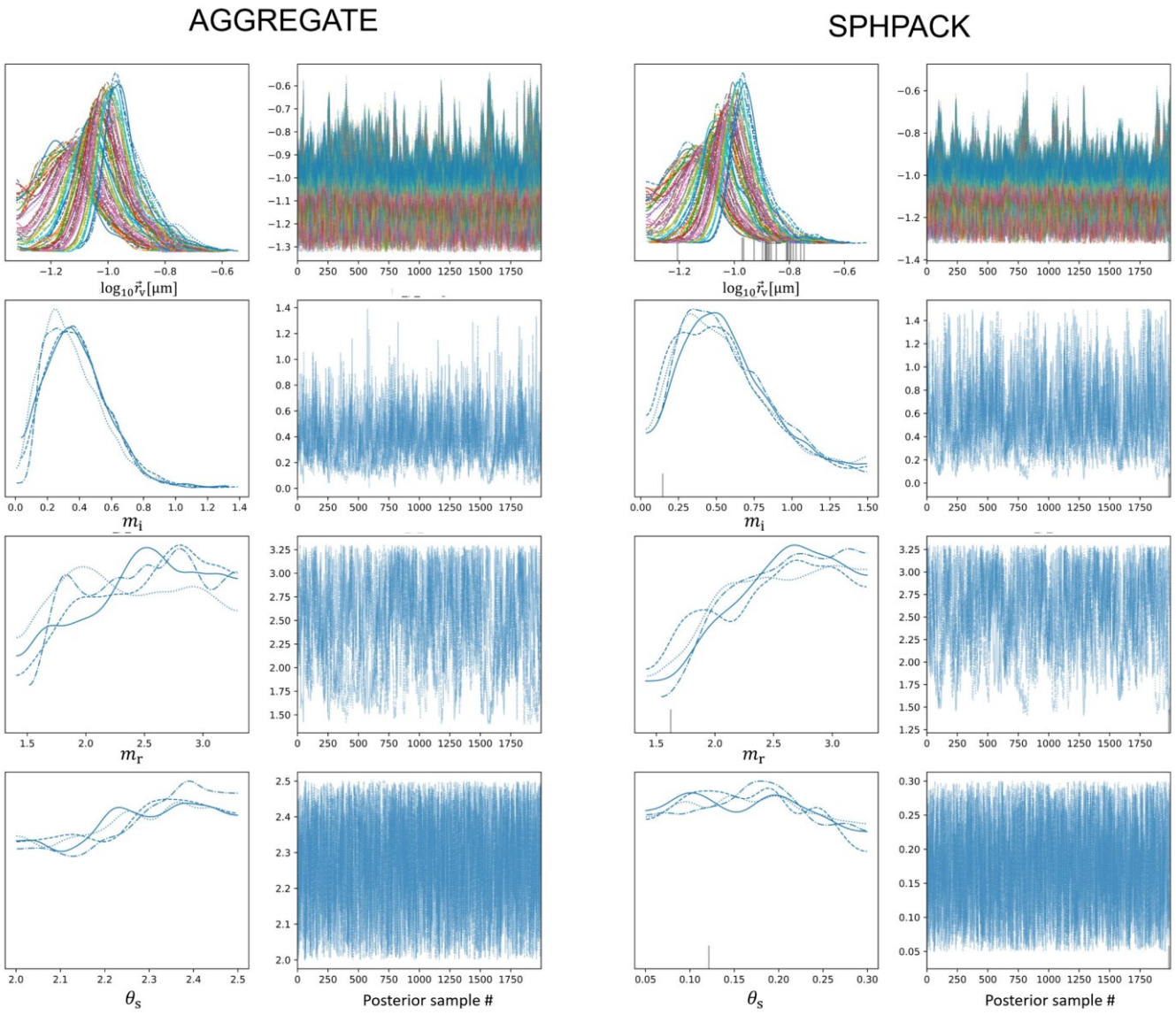

FIG. S9. Same as Figure S6 for Hematite-TD.

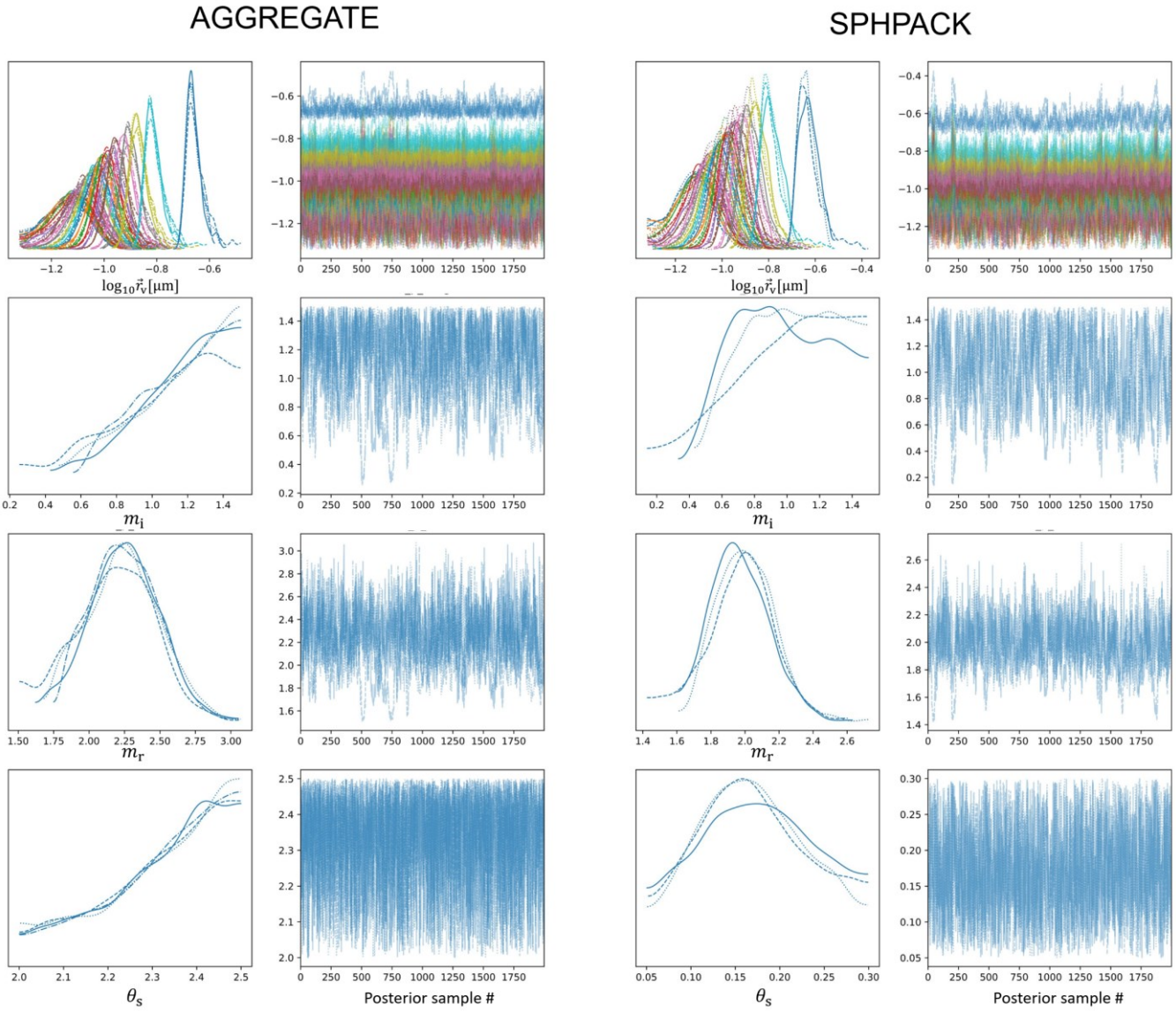

FIG. S10. Same as Figure S6 for ambient BC on July 27th.

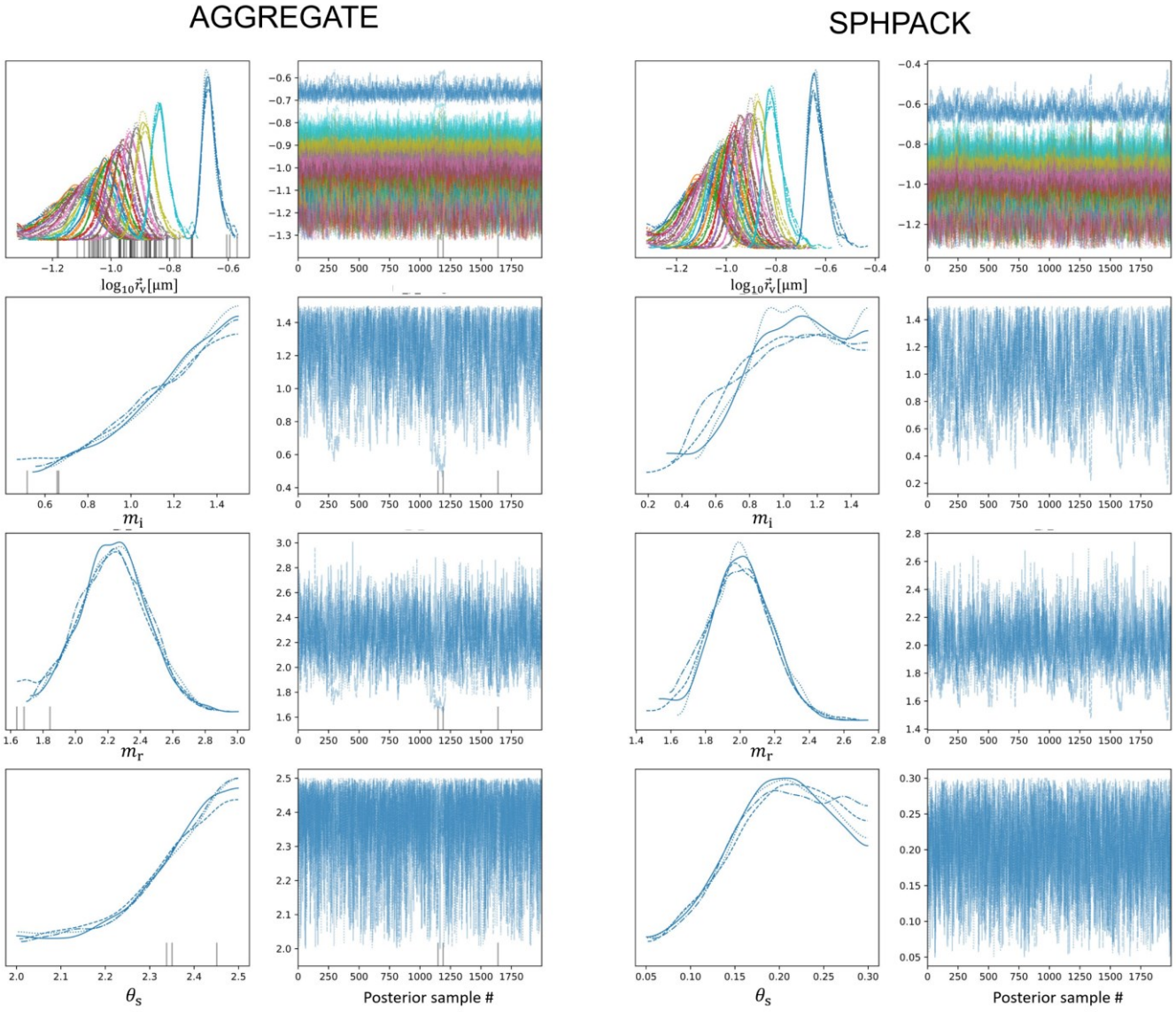

FIG. S11. Same as Figure S6 for ambient BC on July 28th.

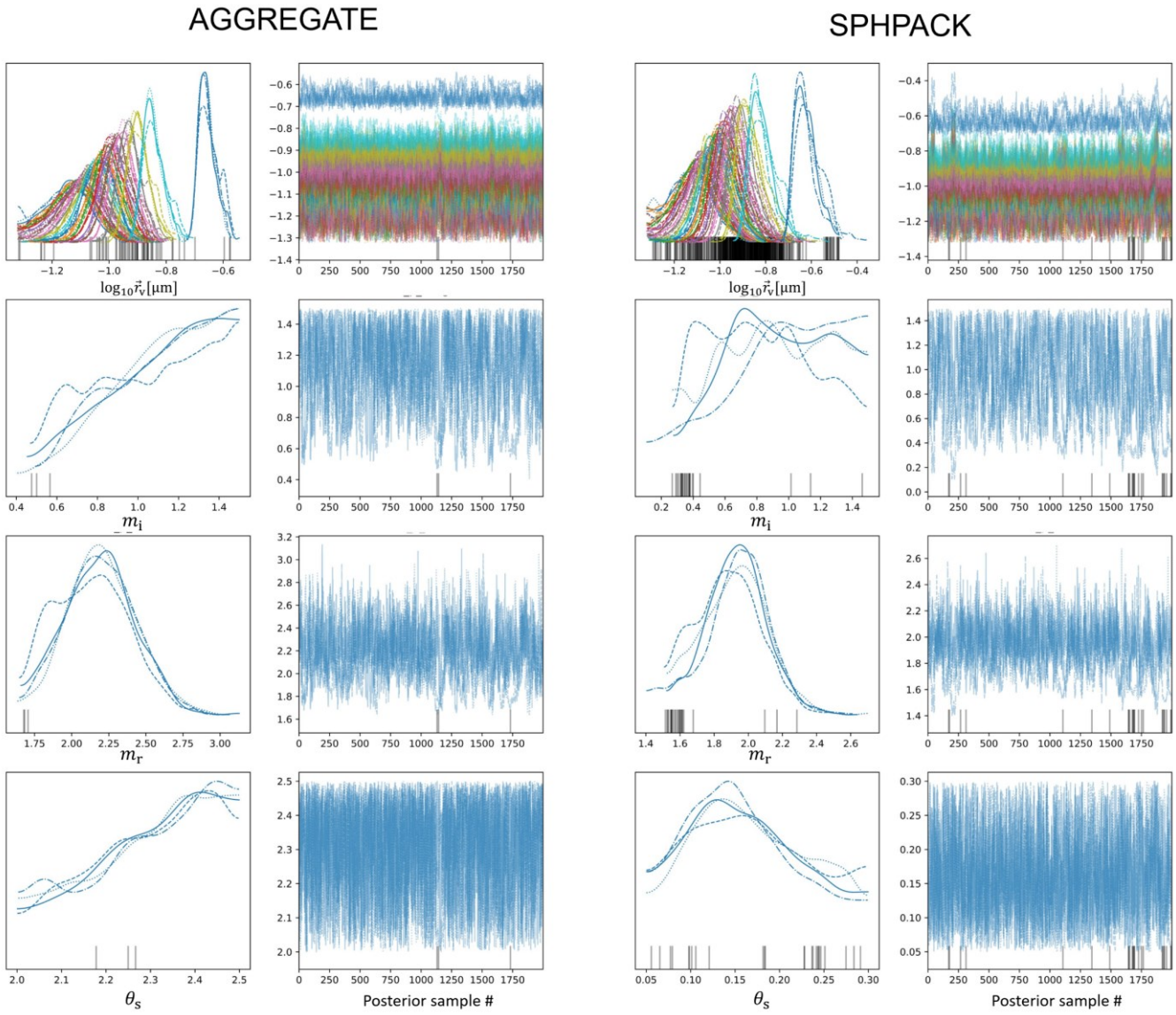

FIG. S12. Same as Figure S6 for ambient BC on July 29th.

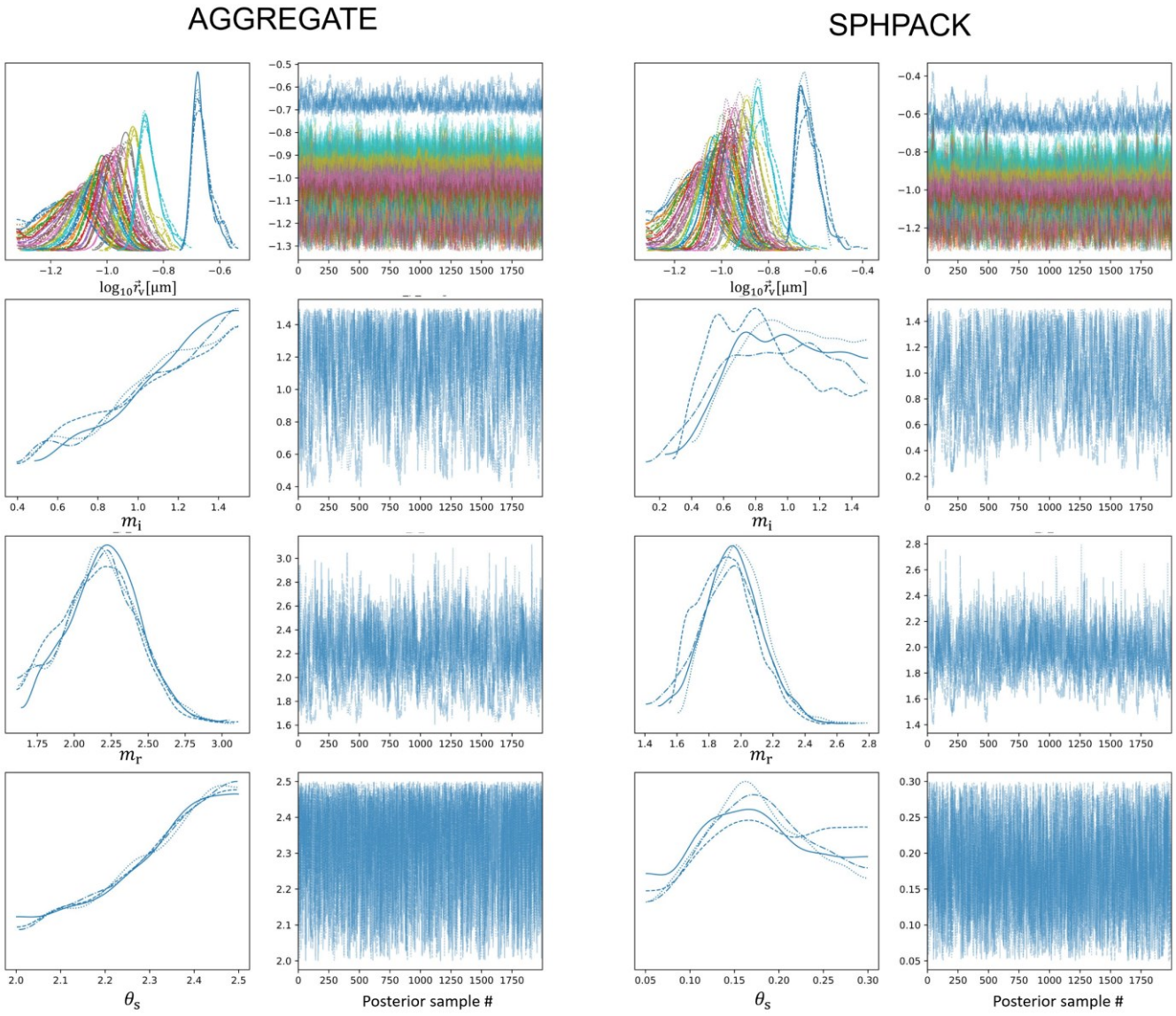

FIG. S13. Same as Figure S7 for ambient BC on July 30th.

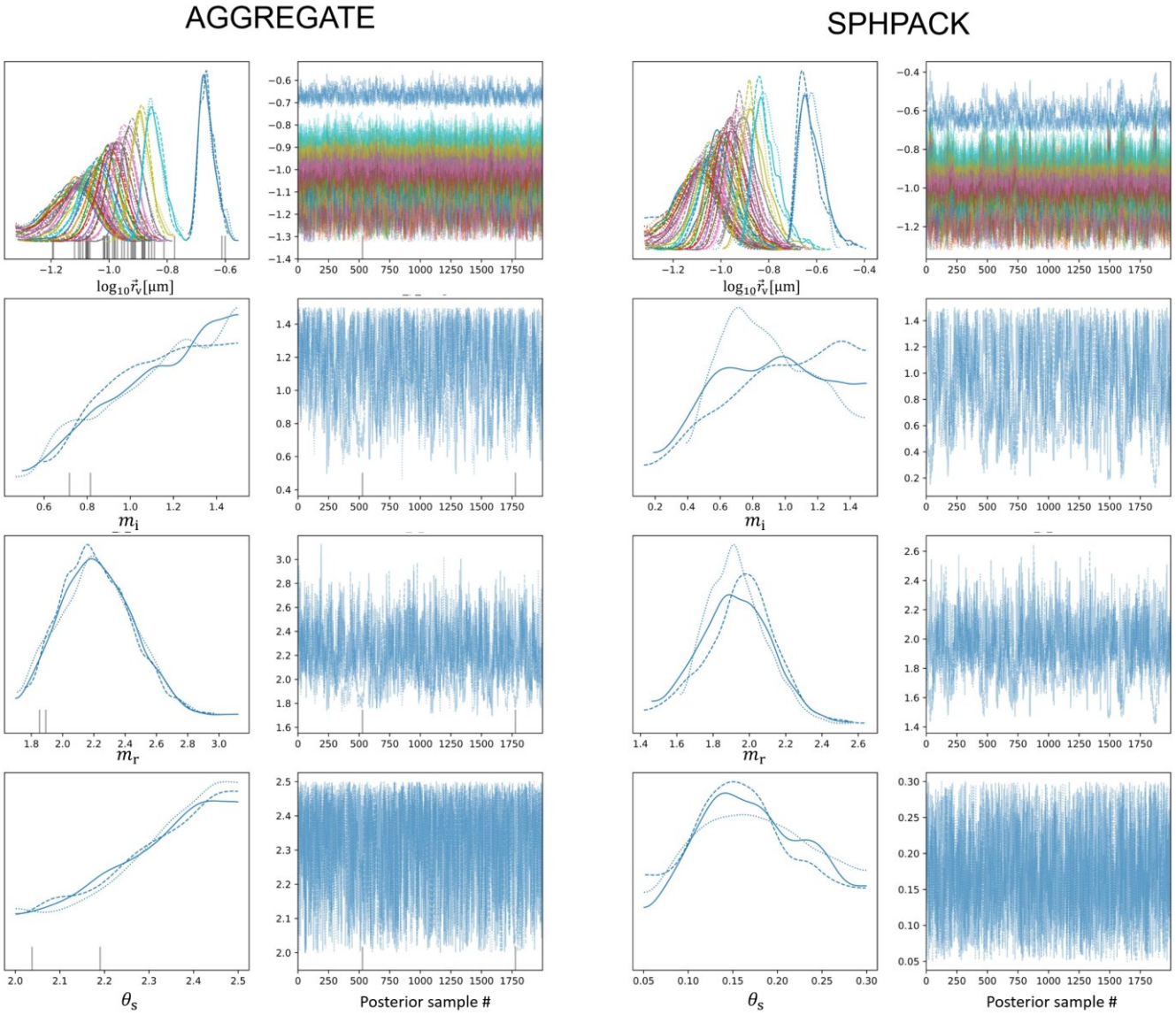

805 **FIG. S14.** Same as Figure S6 for ambient BC on July 31st.

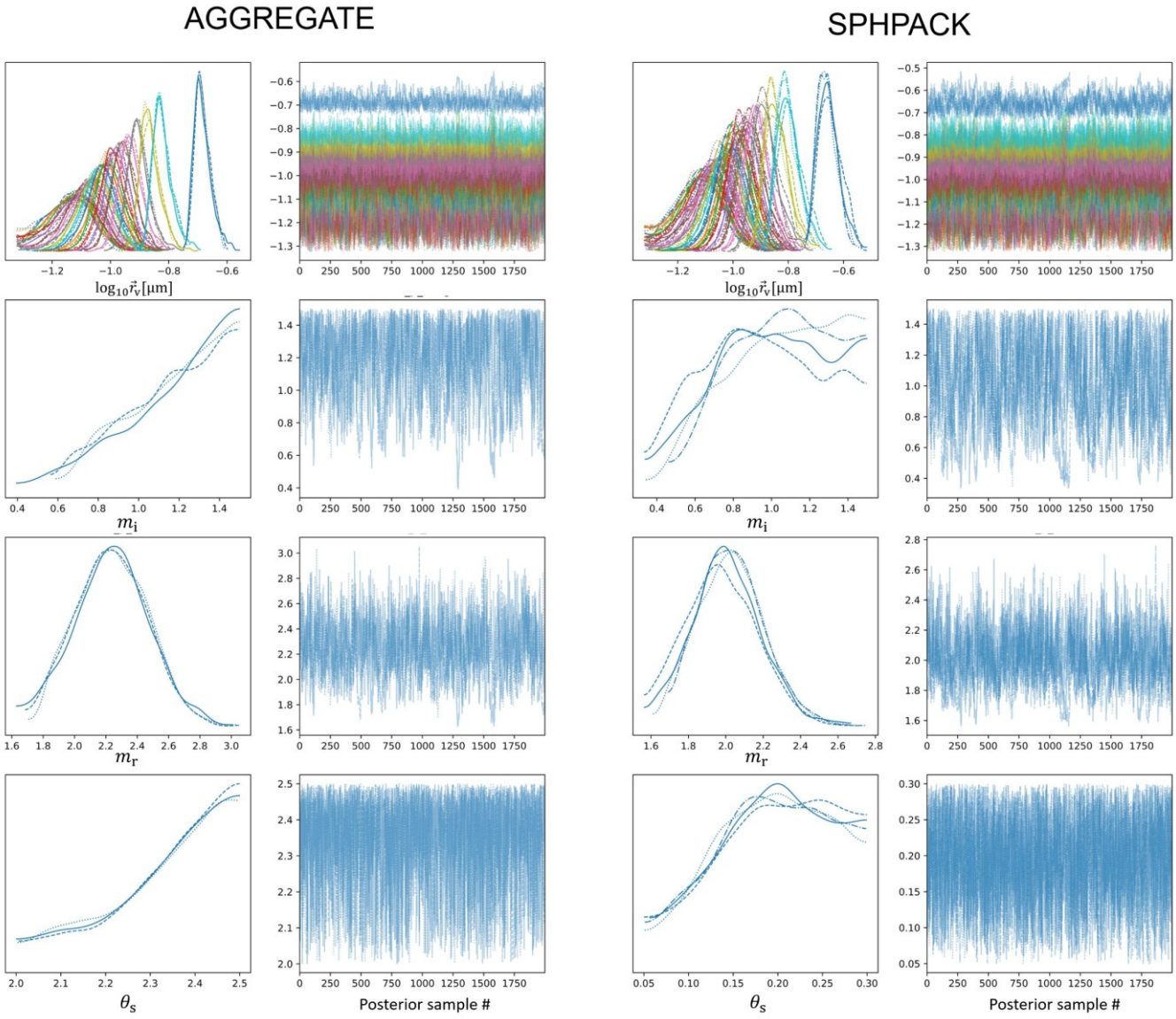

FIG. S15. Same as Figure S6 for ambient BC on August 1st.